Microscopic observations of core-shell particle structure and implications for atmospheric aerosol remote sensing

Florin Unga, M. Choël, Yevgeny Derimian, Karine Deboudt, Oleg Dubovik, Philippe Goloub

AGU100 ADVANCING EARTH AND SPACE SCIENCE

JGR

Journal of Geophysical Research: Atmospheres

RESEARCH ARTICLE

10.1029/2018JD028602

Microscopic Observations of Core-Shell Particle Structure and Implications for Atmospheric Aerosol Remote Sensing

Florin Unga[1,2], Marie Choël[2], Yevgeny Derimian[1], Karine Deboudt[3], Oleg Dubovik[1], and Philippe Goloub[1]

[1]Univ. Lille, CNRS, UMR 8518 - LOA - Laboratoire d'Optique Atmosphérique, Lille, France, [2]Univ. Lille, CNRS, UMR 8516 - LASIR - Laboratoire de Spectrochimie Infrarouge et Raman, Lille, France, [3]Univ. Littoral Côte d'Opale, CNRS, EA 4493 - LPCA - Laboratoire de Physico-Chimie de l'Atmosphère, Dunkerque, France

Key Points:
- About 60% of urban and 20% of desert dust particles presented residuals of coating
- The thickness of shell was found to depend on the size of particle core
- The degree of linear polarization and the scattering in backward directions is sensitive to the aerosol core-shell structure and dimensions

Supporting Information:
- Supporting Information S1

Correspondence to:
F. Unga and Y. Derimian,
florin.unga@univ-lille.fr;
yevgeny.derimian@univ-lille.fr

Citation:
Unga, F., Choël, M., Derimian, Y., Deboudt, K., Dubovik, O., & Goloub, P. (2018). Microscopic observations of core-shell particle structure and implications for atmospheric aerosol remote sensing. *Journal of Geophysical Research: Atmospheres*, *123*, 13,944–13,962. https://doi.org/10.1029/2018JD028602

Received 1 MAR 2018
Accepted 6 NOV 2018
Accepted article online 9 NOV 2018
Published online 28 DEC 2018

Author Contributions:
Conceptualization: Florin Unga, Marie Choël, Yevgeny Derimian
Data curation: Florin Unga, Marie Choël, Yevgeny Derimian
Formal analysis: Florin Unga, Marie Choël, Yevgeny Derimian
Funding acquisition: Marie Choël, Yevgeny Derimian, Philippe Goloub
Investigation: Florin Unga, Marie Choël, Yevgeny Derimian, Philippe Goloub
Methodology: Florin Unga, Marie Choël, Yevgeny Derimian
Resources: Marie Choël, Yevgeny Derimian, Karine Deboudt, Oleg Dubovik, Philippe Goloub
Supervision: Marie Choël, Yevgeny Derimian, Philippe Goloub
Validation: Florin Unga, Marie Choël, Yevgeny Derimian, Philippe Goloub
(continued)

Abstract Although atmospheric aerosol particles can have complex heterogeneous microstructure, simplified homogeneous particle models are often used in remote sensing applications. In this study, the internal structure of individual atmospheric particles was imaged with the aim of parameterizing particle structural heterogeneity. To this end, ambient urban pollution, desert dust, and biomass burning particles were sampled in northern Europe and western Africa and analyzed by transmission electron microscopy coupled with energy dispersive X-ray spectroscopy. Among 8,441 observed particles, about 60% of urban and 20% of desert dust particles presented residuals of coating compounds in the form of a halo surrounding a solid core. Graphic outlining of core and halo areas by image analysis revealed a dependence between halo and core dimensions as well as a greater ratio of halos thickness to total particle diameter (core plus halo) for smaller cores than for larger ones. In the case of urban pollution, the mean ratio for submicrometer and supermicrometer size fractions was 0.25 and 0.19, respectively. The corresponding mean values in the desert dust case were somewhat lower (0.22 and 0.14, respectively), but show a similar decreasing trend. Under the assumption that the halo dimension is proportional to the thickness of the particle shell, the obtained core versus shell dependencies were implemented in numerical calculations of aerosol optical characteristics. Different scenarios of the core-shell dependencies were analyzed with respect to the influence on aerosol optical characteristics, bringing insights into sensitivity to parameterization of the core-shell particle model in remote sensing algorithms.

1. Introduction

Atmospheric aerosols are typically a heterogeneous mixture of particles with different size, shape, and internal structure with various chemical compositions. Electron microscopic observations of thousands of particles can unravel the physical mixing state of atmospheric particles. External as well as internal mixtures of particles were evidenced by numerous studies in different atmospheric conditions (Deboudt et al., 2010; Fan et al., 2016; Hamacher-Barth et al., 2016; Hand et al., 2010; Healy et al., 2013; Marris et al., 2013; Moffet et al., 2010; Pósfai et al., 2013; Pósfai & Buseck, 2010; Sobanska et al., 2014; Young et al., 2016). In particular, the internal structure at the particle scale can take the form of inclusions and coatings (Laskina et al., 2013; Mikhailov et al., 2015) and can represent a significant fraction of investigated atmospheric particles, even outnumbering the homogeneous ones (Li & Shao, 2009a, 2009ab).

The amount of light extinction can be accurately calculated knowing the complex refractive index, the size, the shape, and the mixing state of an ensemble of particles. The assumptions of particle homogeneity and spherical shape are the common simplifications enabling fast computations with a minimal number of variables. However, the physical mixing state and the shape of particles can strongly affect their optical properties. For instance, the influence of particle shape on atmospheric aerosol optical characteristics is modeled by an ensemble of randomly oriented spheroids (Dubovik et al., 2006; Mishchenko & Travis, 1994) and is presented in remote sensing algorithms as distribution of aspect ratios and fractions of spherical and nonspherical particles (Dubovik et al., 2006). The internal structure at the particle scale can also produce important features of optical characteristics (Fuller, 1995; Fuller & Kreidenweis, 1999). The absorption and scattering properties of an ensemble of aerosol particles are strongly dependent on the mixing scenario used, either external or internal (Bond et al., 2006; Lesins et al., 2002; Liu et al., 2014; Ramachandran & Srivastava, 2013).

Visualization: Florin Unga, Marie Choël, Yevgeny Derimian
Writing - original draft: Florin Unga
Writing – review & editing: Florin Unga, Marie Choël, Yevgeny Derimian, Karine Deboudt

Some models treat the internally mixed components assuming a particle is composed of a homogeneous mixture of different species; thus, the complex refractive index of two or more components are mixed based on one of the effective medium approximation rules, for example, Maxwell-Garnett theory, Bruggeman theory, and volume weighted (Easter et al., 2004; K. Zhang et al., 2012). Another commonly used model of the internal structure is the concentric multilayered particles (Stamnes et al., 1988; Yang et al., 2002). For instance, previous calculations have shown that the absorption is enhanced when a nonabsorbing material coats a soot particle (Bond et al., 2006; Cappa et al., 2012; Kahnert, 2015; Mishchenko et al., 2014; Schwarz et al., 2008). Furthermore, changes in optical properties have been discussed by Bauer et al. (2007) for the case of mineral dust coated with sulfate and nitrate secondary products. The influence of structural inhomogeneity has also been the subject of studies in laboratory (Lang-Yona et al., 2010) and in remote sensing observations (Derimian et al., 2017; Li et al., 2013; Schuster et al., 2009). However, in contrast to the particle shape effect, the internal structure of particles is not considered in aerosol remote sensing applications.

In this study, we report microscopic observations of core-shell particles sampled in different regions and environmental conditions. These core-shell structures are typically formed when aerosol particles interact with water vapor and/or various reactive gaseous species during their transport in the atmosphere. This involves gas condensation and/or heterogeneous reactions at the particle surface. We specifically investigate core-shell particles collected in an urban environment during a particulate pollution event and in a desert environment during biomass burning intrusion. Such events favor the formation of core-shell structures (Laskin et al., 2016; Niu et al., 2015; Tang et al., 2016). This study therefore relies on two field campaigns conducted in northern France and western Africa, Senegal, in order to investigate whether a parameterization of the core-shell structure is possible. We then illustrate how aerosol optical characteristics change for representative particle size distributions, as a function of core-shell dimensions and chemical composition.

2. Materials and Methods

2.1. Sampling Sites

Intensive field observations were carried out in the metropolitan area of Lille, northern France (50°36′29″N, 3°8′25″E), during a particulate pollution event occurred in March 2014 affecting northwestern Europe with markedly elevated particulate matter (PM) concentrations (Elliot et al., 2016; Smith et al., 2015; Vieno et al., 2016). The Lille site, hereafter referred to as *urban environment*, is a long-term AERONET site (Holben et al., 1998) equipped with a micro-Lidar (CIMEL Electronique S.A.S). Additional description of the site can be found in Bovchaliuk et al. (2016) and Mortier et al. (2013).

SHADOW (SaHaran Dust Over West Africa) campaign was carried out from March to April 2015 and from December 2015 to January 2016 in the coastal city of Mbour, Senegal, western Africa (14°23′38″N, 16°57′32″W), located 80 km south of Dakar. This campaign aimed at investigating the microphysical and microchemical properties of desert dust outbreaks and biomass burning intrusions. More details on this campaign can be found elsewhere (Bovchaliuk et al., 2016; Péré et al., 2018; Rivellini et al., 2017; Veselovskii et al., 2016). The Mbour site, hereafter referred to as *desert environment*, is a long-term AERONET site (named Dakar in AERONET), which is equipped with a CIMEL micro-Lidar (Mortier et al., 2016).

Airborne particles were collected within the transported dust and biomass aerosol layers. The same impactor and collection substrate were used in both sampling campaigns. Atmospheric particles were collected using a 4-stage personal cascade impactor (Sioutas, SKC Inc.) at a flow rate of 9 L/min (Singh et al., 2003). The size segregation of particles was according to the following aerodynamic diameter (d_{aer}) ranges: $d_{aer} > 2.5$ μm; $1.0 < d_{aer} < 2.5$ μm; $0.50 < d_{aer} < 1.0$ μm; and $0.25 < d_{aer} < 0.50$ μm. Particles were impacted onto Formvar/Carbon coated 200 mesh copper transmission electron microscope (TEM) grids (Ted Pella Inc.). More details about particle samplings are provided in the supporting information.

2.2. Transmission Electron Microscopy

TEM has been proven to be a suitable technique for providing information on structure, morphology, and chemical composition of individual particles (Adachi et al., 2010; Adachi & Buseck, 2013; Laskin et al., 2006; Li et al., 2011; Pósfai et al., 2013; Verleysen et al., 2014). However, some compounds, especially volatile species, are prone to degradation in the high vacuum conditions of the TEM (Pósfai et al., 1998; Reid, Eck, et al., 2005). This effect strongly depends on the composition of aerosol particles. Refractory

compounds, such as fresh soot, mineral dust, or metallic particles remain unchanged, while semivolatile and water soluble compounds are evaporated within the high vacuum chamber of TEM. Moreover, some particles are vulnerable to radiation damage caused by the incident electrons. To avoid this effect, we initially acquired electron micrographs of particles from the entire grid, prior to energy dispersive X-ray (EDX) analysis of particles. In the case of core-shell particles, the coating compounds form a halo. During EDX analysis, the beam rasters the core only, because the spectra of the halo cannot be acquired due to the low material remaining after evaporation in the vacuum of the microscope chamber. This fact, together with the circular appearance of the halo, indicates that most of the particle coating was composed of volatile liquids. Our observations are in line with an experiment conducted by Pósfai et al. (1998) on liquid particles impacted on the same type of substrate as in our work. In this experiment, the cross-sectional atomic force microscopy profiling evidenced particles with a hemispherical shape after impaction. Subsequent observation of the same particles by TEM revealed that volume loss (mostly water or semivolatile compounds) occurred along with vacuum in the TEM chamber and a residue is left, forming circular halos on the substrate around the dried particles. The particle drying in TEM is taken here as an advantage for revealing the refractory core inside a halo composed of liquid shell residuals. Individual particles were examined using a TEM (Tecnai G2-20, FEI) operating at 200 kV accelerating voltage (LaB6 filament) fitted with a Gatan ORIUS SC1000 CCD camera. The elemental composition of particles was determined using an EDX spectrometer (EDAX Inc.) with a Si (Li) thin window detector having an active surface of 30 mm^2 and an energy resolution of 136 eV (for MnK_α).

2.3. Image Analysis

TEM images were processed using FIJI (Schindelin et al., 2012) based on ImageJ (Schneider et al., 2012). This software package is commonly used for counting and measuring the surface area of atmospheric particles imaged by electron microscopes (Bescond et al., 2014; Huffman et al., 2012; Rocha-Lima et al., 2014). Using this tool, the projected surface area of halo residual and core of particles was measured, assuming that they are proportional to the cross section of real atmospheric particles. Such methodology was applied also by Chou et al. (2008), Hamacher-Barth et al. (2013), Li and Shao (2009a, 2009ab), and Pósfai et al. (2003). For quantifying the particle internal structure, the particle projected surface area was measured by counting the number of pixels comprised in 2-D-projected particle. To ensure accurate measurements, a series of image treatments were necessary, by manually adjusting the contrast and brightness of each electron micrograph according to the gray level threshold. To evaluate the accuracy of surface area measurements, particles of different sizes were digitalized at different magnifications up to 70,000X. A maximum of 2% difference in measured surface area at different magnifications was estimated. A typical electron micrograph and the corresponding treated image are presented in Figure 1. Some particles were excluded from the analysis due to the lack of clear contrast between the gray level of core and halo, for example, the particle marked with a green arrow in Figure 1a.

Considering that the projected area of a particle ($A_{proj.\ core,\ total}$) is equal to the area of a circle that covers the same surface, one can calculate an equivalent diameter of the core (d_{core}) or of the total diameter of core plus halo (d_{total}). The thickness of halo (Δ_{halo}) can be defined as follows:

$$\Delta_{halo} = \frac{d_{total} - d_{core}}{2}. \quad (1)$$

The particle image analysis provides also Feret's diameters (denoted as F_{max} and F_{min}), which are defined as the maximum and minimum caliper, respectively. We can therefore calculate the ratio between F_{max} and F_{min} to obtain the particle axis ratio describing the shape of particles.

3. Results and Discussions

3.1. Description of the Case Study Events

The urban pollution sampling was conducted during a widespread pollution episode occurred in northwestern Europe in March 2014 (Elliot et al., 2016; Smith et al., 2015; Vieno et al., 2016). This pollution event was reported to cause ~600 deaths and ~1,500 emergency hospitalizations in the United Kingdom (Macintyre et al., 2016). Atmospheric particulate matter was collected on 13 March in a near-ground pollution layer

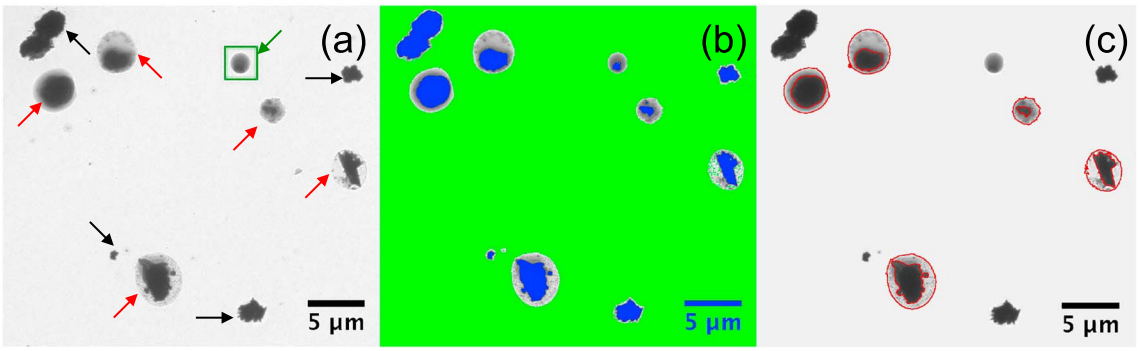

Figure 1. Illustration of the methodology for graphic outlining of the particle surface area: (a) electron micrograph of particles, where black arrows show uncoated particles, red arrows show coated particles, green arrow shows an example of a particle excluded from the analysis due to the lack of clear contrast; (b) threshold micrograph, where blue, gray, and green colors represent the core, the residual halo, and the background, respectively; (c) the selected cores and residual halos contoured by red line.

where PM mass was dominated by $PM_{2.5}$ representing 86% of PM_{10}. The detailed optical and in situ measurements conducted during this episode are presented in Figure S1 accompanied by the references thereby (Dubovik, Holben, Eck, et al., 2002; Eck et al., 1999; Mortier et al., 2013).

The desert dust event with biomass burning intrusion occurred during the dry season, when the biomass burning aerosol from anthropogenic activities in Sahelian and sub-Sahelian regions frequently reach the site (Hand et al., 2010; Haywood et al., 2008; Osborne et al., 2008) and are transported over a dust layer (Léon et al., 2009; Mortier et al., 2016). Aerosols were sampled on 20 January 2016 at 3.7 km altitude in an atmospheric layer where biomass burning particles were mixed with desert dust. This event is described in details in Figures S2 and S3 complemented by the references thereby (Deboudt et al., 2010; Engelhart et al., 2011; Fard et al., 2017; Flament et al., 2011; Kreidenweis et al., 2008; Mortier et al., 2016; Nguyen et al., 2016; Tan et al., 2017).

The differences in the aerosol microphysical and optical properties during the two case studies are illustrated by the AERONET derived column integrated size distributions (Figure 2a), the spectral single scattering albedo (SSA; Figure 2b) and the lidar derived vertical profiles of extinction coefficient (Figure 2c). In the case of urban pollution, the fine mode dominates the size distribution. In the case of desert dust event with biomass burning intrusions, the volume size distribution is characterized by practically equal fine and coarse modes representing a mixed aerosol type. The fine mode urban particles ($r_{mode\ fine}$ = 0.25 µm) are larger than the fine mode particles from the case of the desert dust and biomass burning mixture ($r_{mode\ fine}$ = 0.08 µm). The SSA of about 0.9 in the case of urban environment shows that the

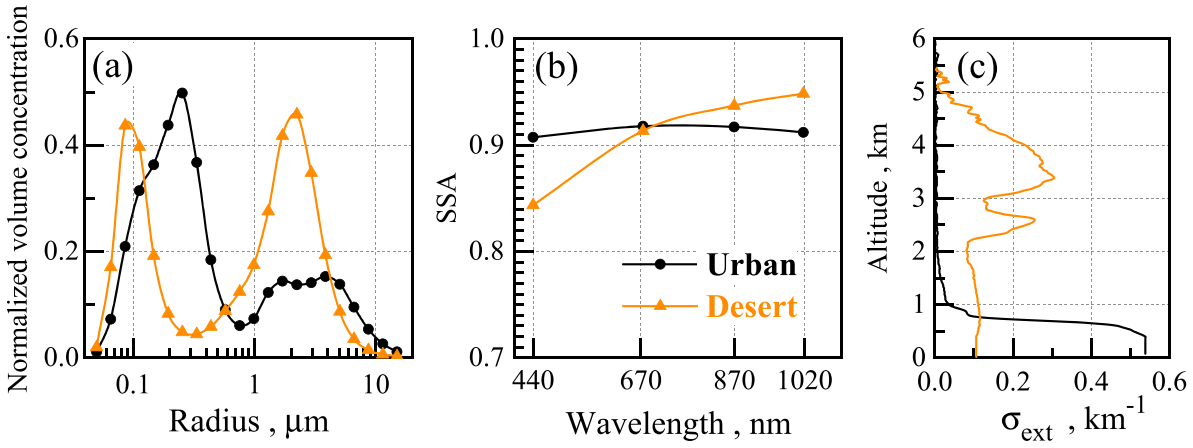

Figure 2. Comparisons of AERONET derived (a) size distribution normalized to the total volume concentrations, (b) spectral SSA, and (c) lidar derived extinction profiles for sampling in urban and desert environments represented with black and orange lines, respectively. SSA = single scattering albedo.

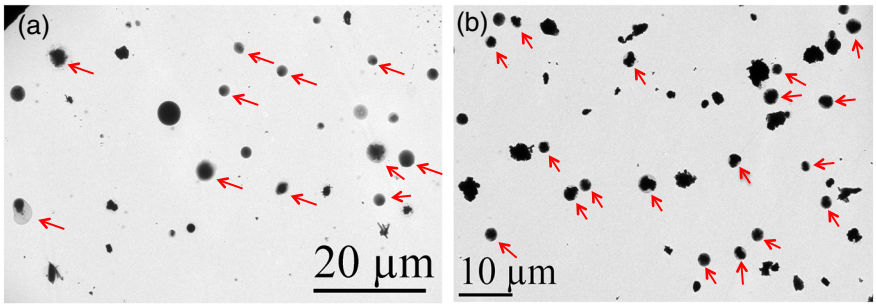

Figure 3. Overview of particles collected in $1.0 < d_{aer} < 2.5$ µm size fraction (a) in urban environment and (b) in desert environment during biomass burning intrusion. Red arrows point to particles that present a halo.

aerosols are low light-absorbing. In the case of desert environment, a stronger absorption appears at shorter wavelengths, which is typical for desert dust due to the presence of iron oxides. At the same time, the values are quite low (~0.85), which can be explained by the presence of biomass burning, known to be more light-absorbing (Reid, Eck, et al., 2005; Reid, Koppmann, et al., 2005). The extinction profile in the case of urban environment shows that the aerosols are concentrated in the lower part of the troposphere (Figure 2c), while in desert environment, the extinction profile indicates transport of two aerosol layers at altitudes of about 2 to 3 and 3 to 5 km.

3.2. Physicochemical Characteristics of Core-Shell Particles

Figure 3 presents electron micrographs of typical particles collected in urban and desert environments. Observed particles were categorized in two groups, those that present a halo (identified by red arrows) and those without halo, representing coated and not coated particles, respectively. Hereafter, particles that present a halo are termed *coated urban particles* and *coated desert particles*.

An overview of particles collected in the urban and desert environments is presented in Figures S4 and S5. Coating of atmospheric particles is often resulting from enhanced hygroscopicity due to aging mechanisms such as coagulation, condensation, and heterogeneous chemical reactions (Khalizov et al., 2009; Moffet et al., 2010; Müller et al., 2017). Presence of coating was reported in numerous studies in urban agglomerations (Li & Shao, 2009a, 2009ab; Niemi et al., 2006; Niu et al., 2015; Pirjola et al., 2017) and desert environments (Derimian et al., 2017; Kandler et al., 2007; Laskin et al., 2005). A previous study by Deboudt et al. (2010) of the particle mixing state at the Mbour site showed that marine and carbonaceous compounds can form coatings on mineral dust particles.

Figures 4 and 5 present electron micrographs of individual particles collected in urban and desert environments, respectively. Sixty-one urban particles and 73 desert particles, randomly chosen from all four aerodynamic diameter ranges, were chemically analyzed. Among them, 36 urban and 29 desert particles presented a halo. The major elements common to studied particles were C, O, S, Na, K, Ca, Al, Si, Fe, Cr, and Ni. The sample from the urban pollution event additionally contained Mn and Zn. The sample from the dust event with biomass burning intrusion additionally contained P and Ti. Based on their main elemental composition, all the analyzed particles were sorted into eight groups: (1) Al/Si-rich; (2) Al-rich (particles exclusively found in the urban pollution sample) or Si-rich (particles exclusively found in the desert dust sample); (3) Ca-rich; (4) transition metal-rich (Fe, Cr, Ni, also containing Ti-rich particles in the desert dust sample, and Mn-Zn-rich particles in the urban pollution sample); (5) C/S/K-rich (also containing P for particles from the desert dust sample); (6) Na-rich; (7) soot; and (8) tar balls.

3.2.1. Urban Particles

Particles with coating residuals were found in all particle types except tar balls.

(1) **Al/Si-rich** particles can also contain Ca, Mg, and Fe. Their shape was mostly angular (Figures 4a and 4b), which indicates soil erosion origin (Choël et al., 2007). Coated Al/Si-rich particles were also found (Figure 4b) with variable traces of S, which suggests aging processes with S-containing species, most probably as a result of surface coagulation and condensation (Fan et al., 2016; Li & Shao, 2009a, 2009ab; Sullivan et al., 2007). In addition, some Al/Si-rich particles also contained traces of K (not shown),

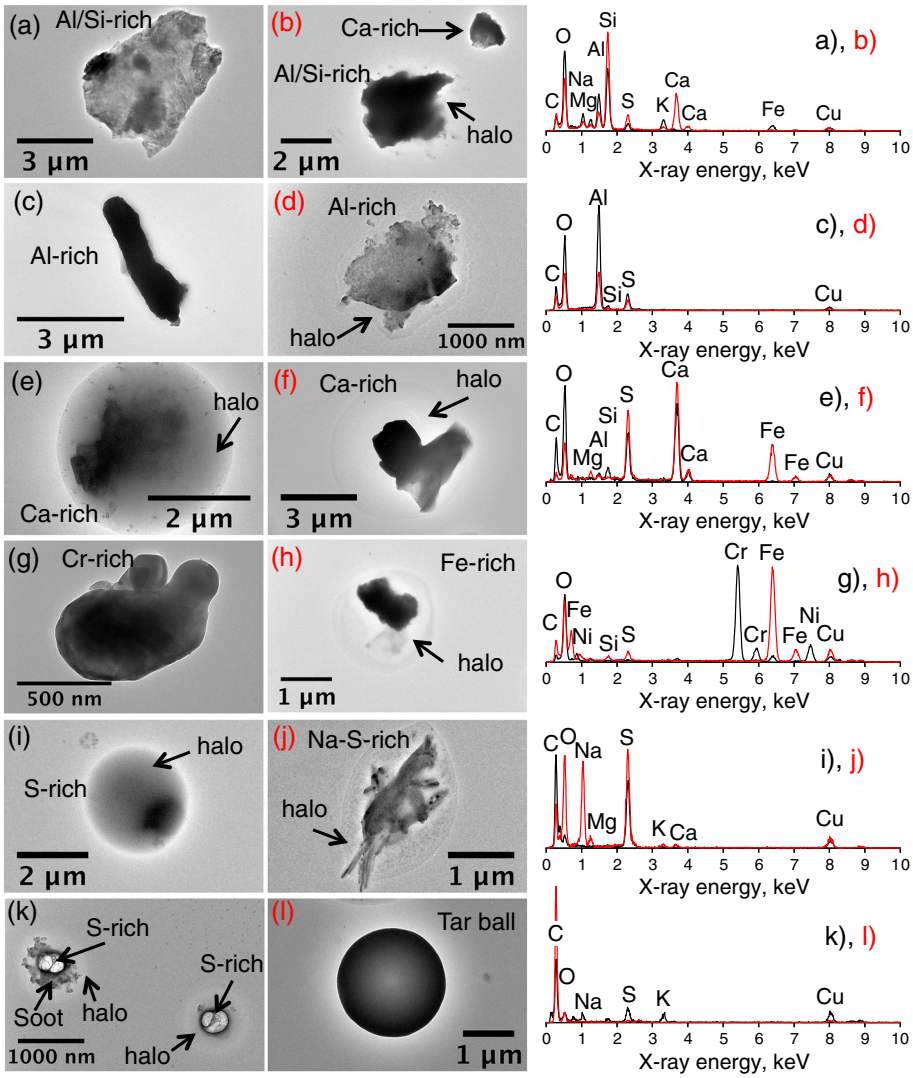

Figure 4. Electron micrographs of urban particles and their corresponding energy dispersive X-ray spectra of (a) AlSi-rich, (b) AlSi-rich with halo and Ca-rich, (c) Al-rich, (d) Al-rich with halo, (e, f) Ca-rich with halo, (g) Cr-rich, (h) Fe-rich with halo, (i) S-rich with halo, (j) Na-S-rich with halo, (k) soot attached to S-rich with halo, and (l) tar ball particles.

which are markers of biomass burning most probably from residential wood heating. (2) **Al-rich** particles contained S or Si as minor elements. They have an elongated shape (Figure 4c) and some of them were encapsulated into a host (Figure 4d). They most probably originate from soil dust (Shi et al., 2009) or anthropogenic emissions (Hoflich et al., 2005). (3) **Ca-rich** particles were found with high O and S contents and were sometimes mixed with Al/Si. Some of them presented minor traces of Fe, Mg, P, Na, K, and occasionally Zn. A Ca-rich particle with no halo is illustrated in Figure 4b (upper right particle). The coated Ca-rich particles have angular shapes and circular halo (Figures 4e and 4f). (4) **Transition metal-rich** particles were subcategorized into Zn-Mn-Cr-Ni-rich (Figure 4g) and Fe-rich particles. The Zn-Mn-Cr-Ni-rich with abundant O presented also traces of Fe, Mg, Al, Si, P, and K. These particles may result from tailpipe exhaust, roadway dust, residual of heating fuels but also from brakes and tire abrasions. Another potential source may be from the subway wheels and trails, which are located at a distance of few hundred meters near the urban sampling site. Fe-rich particles had high O content and some of them presented traces of S, P, Na, Mg, Al, Si, K, Ca, Mn, Zn, and Cl. Some Fe-rich particles presented angular shapes and a circular residual halo (Figure 4h). Pure Fe-rich particles have been found to have circular shape. (5) **C/S/P/K-rich** particles include particles rich in C (but not having the shape

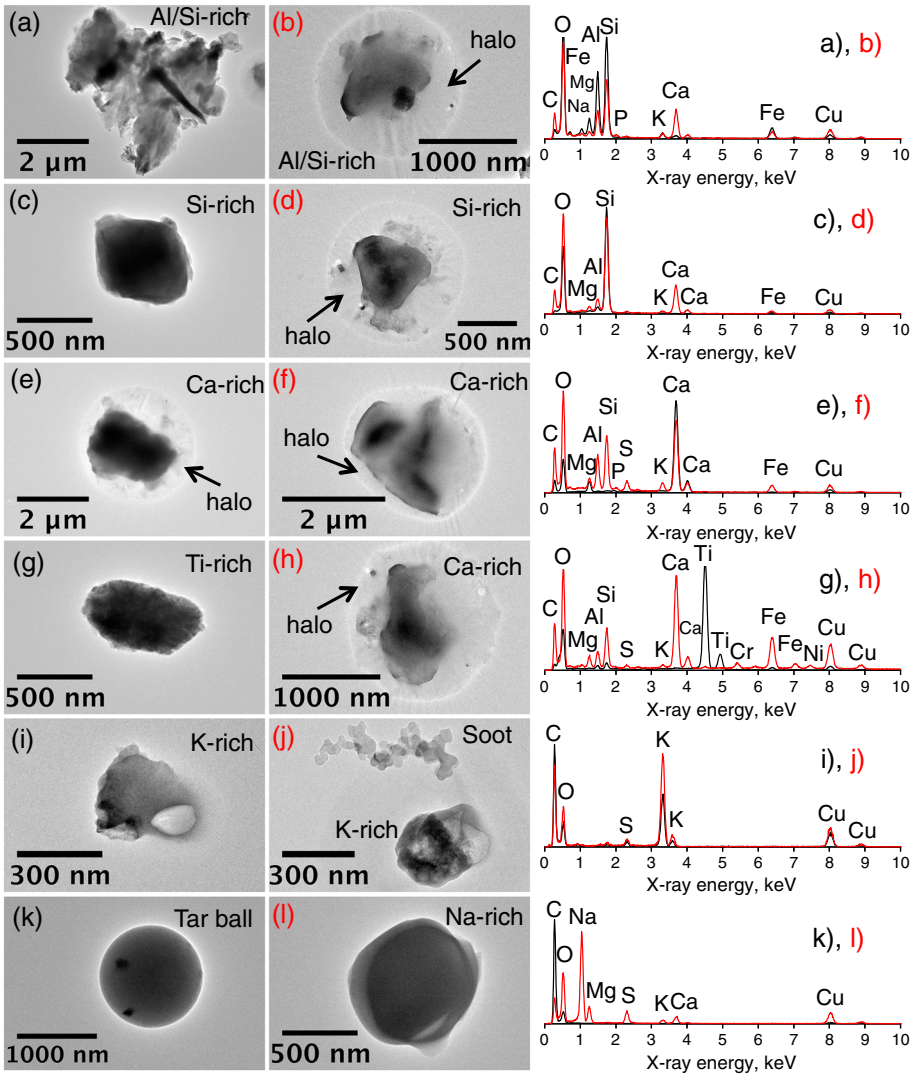

Figure 5. Electron micrographs and corresponding energy dispersive X-ray spectra of particles collected at 3.7 km altitude in desert environment during biomass burning event: (a) Al/Si-rich, (b) Al/Si-rich with halo, (c) Si-rich, (d) Si-rich with halo, (e, f, and h) Ca-rich with halo, (g) Ti-rich, (i) K-rich, (j) soot and K-rich, (k) tar ball, and (l) Na-rich particles.

of nanospheres aggregates as soot) or S or P or K or combinations of two or three elements and some of them presented minor Mg (Figure 4i). This category of particles is considered as markers of wood combustion processes. Some particles from this category were strongly beam-sensitive. (6) **Na-rich** particles such as aged sea spray aerosol originating most probably from the northwestern coast of France were also found (Figure 4j). The corresponding X-ray spectrum displays minor K and Ca peaks as well as an intensity ratio of Na to Mg (10:1) matching the elemental ratios reported for aged sea spray particles in the southeast United States by Bondy, Wang, et al. (2017). The halo in this case could be of marine origin. (7) **Soot** particles are mostly distinguishable by their form of chain-like aggregates of nanospheres. In addition to C, some of them contained minor traces of S and/or Si. They are emitted by various pollution sources such as diesel exhaust, industrial emissions, and domestic fires (Fan et al., 2016). These particles can evolve by condensation and coagulation with sulfates and water-like compounds (Johnson et al., 2005; Niemi et al., 2006; Pirjola et al., 2017). Some soot particles have been found internally mixed with sulfate and presented a circular halo (Figure 4k). (8) **Tar balls** are round carbonaceous particles stable under the electron beam (Figure 4l). They usually originate from smoldering burning combustion (Chakrabarty et al., 2010).

3.2.2. Particles in Desert Environment Under Biomass Burning Intrusion

Contrary to urban particles, only particles from aluminosilicate-rich, silicate-rich, and Ca-rich types were observed with residuals of coating compounds.

(1) **Al/Si-rich** particles presented irregular shapes (Figure 5a) and some of them presented residuals of liquid coating compounds (Figure 5b). These Al/Si-rich particles presented traces of Ca, Mg, Fe, Na, P, K, S, and Ti. Based on the classification from Chou et al. (2008), aluminosilicate particles were mostly feldspar (intensity ratio Si/Al ~3), illite (Si/Al $>$ 2) and kaolinite (Si/Al ~1). (2) **Si-rich** particles contained traces of Fe, Mg, Ca, Na, Mg, S, and K. They presented angular shapes. Quartz particles were observed without halo (Figure 5c) and with halo (Figure 5d). (3) **Ca-rich** particles were mostly found with halo (Figures 5e, 5f, and 5h). These particles contained traces of S, K, P, Na, Fe, Mg, Ti, Mn, and Ni. Calcium-rich particles can be in the form of calcium carbonate ($CaCO_3$) and dolomite ($CaMg(CO_3)_2$). During transport, they could be partially converted into calcium nitrate followed by the deliquescence of the calcium nitrate product (Krueger, 2003). The deliquescent calcium nitrate shell could have formed a halo upon dehydration in the TEM chamber. (4) **Transition metal-rich** particles (Ti-rich, Zn-rich, and Fe-rich) were found without halo (Figure 5g). (5) **C/S/K-rich** particles (Figures 5i and 5j) are carbonaceous particles with inorganic K-sulfate inclusions typically found in biomass smoke. They have a rounded morphology, did not present a halo, and were beam-sensitive. (6) **Soot** particles easily identified in the form of nanospheres aggregated together in a chain-like structure were observed (Figure 5j). (7) **Tar balls** are other carbonaceous particles that are resistant to electron beam damage with a characteristic spherical shape typical of wildfire emissions (China et al., 2013; Figure 5k). (8) **Na-rich** particles contained low amount of Cl, indicating aged sea-salt particles converted to sodium nitrate and sodium sulfate (Figure 5l). They were highly sensitive to beam damage.

Biomass burning particles sampled in desert environment were found predominant in the submicrometer size fractions. Desert dust was found more abundant in the supermicrometer size fractions. Indeed, desert dust particles may be transformed during transport through multiphase chemistry, resulting in internal mixing with condensed-phase organic constituents (Laskin et al., 2016). Nitrates and sulfates can uptake onto mineral dust by forming a layer around the particle and transforming the shape of the nonspherical mineral dust into a spherical one (Hwang & Ro, 2006; Kojima et al., 2006; Laskin et al., 2005; Li & Shao, 2009a, 2009ab; Matsuki et al., 2005; Sullivan et al., 2007; Tang et al., 2016; D. Zhang et al., 2000). The presence of K and S in dust particles could indicate coatings of mineral desert dust with K-sulfate, which is a marker of biomass burning.

3.3. Dependence Between Dimensions of Core and Size of Halo

TEM observations of 8,531 particles were used to describe their internal structure at individual particle scale. Among the 2,569 observed particles in urban environment, 60% presented a halo. In desert environment, among the 5,872 observed particles, 20% presented a halo. The data can be accessed from Unga (2018). The number size distribution of the particles presenting a halo is presented in Figure 6: as the size fraction becomes smaller, the relative shift in the particle size due to the presence of halo becomes systematically larger, that is, the relative shift of the mode diameter (δ). It indicates that the smaller particles tend to have larger halos for both urban and desert dust cases. However, the width of the size distribution in the case of urban particles is notably larger than that of desert dust particles due to differing particle types, as described in section 3.2.

The study of the halo thickness (Δ_{halo}) according to the core size (d_{core}) confirms a clear dependency between the dimensions of cores and halos (Figure 7). In general, for both urban and desert dust particles, Δ_{halo} increases with d_{core} but the slope of the increase is steeper for smaller d_{core} (see also insert table in Figure 7). It is notable that the mean Δ_{halo} for urban particles is higher than the one for desert particles. At the same time, the dispersion of Δ_{halo} is higher in the case of urban particles than in the case of desert particles (~0.4 vs ~0.3, respectively). This larger dispersion can be due to a more variable aerosol composition that affects the particle shell, for example, Laskina et al. (2015). Indeed, if we assume that the halo size is proportional to the thickness of particle shell (material surrounding a particle before it was sampled on the substrate), then a larger relative dispersion of Δ_{halo} is in line with the stronger diversity of chemical composition of urban particles. The thickness of halo is also expected to vary according to the chemical composition of shells themselves. Thus, the chemical composition of shells, along with the chemical composition of cores, is expected to contribute to the dispersion of Δ_{halo} as a function of d_{core}. Other factors such as relative

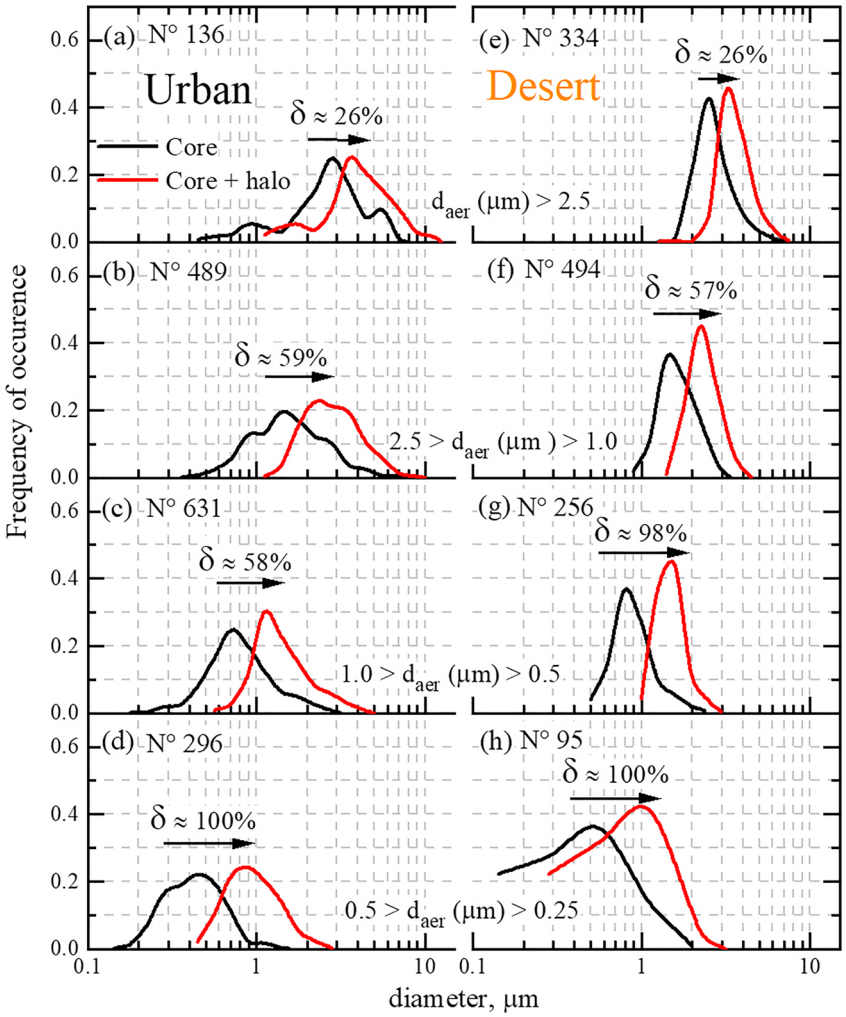

Figure 6. Number size distributions normalized to the total number of particles in (a), (e) $d_{aer} > 2.5$ μm, (b), (f) $1.0 < d_{aer} < 2.5$ μm, (c), (g) $0.50 < d_{aer} < 1.0$ μm, and (d), (h) $0.25 < d_{aer} < 0.50$ μm size fractions. Left and right columns correspond to sampling in urban and desert environment, respectively. Black and red lines represent the distributions for core and core plus halo diameters, respectively. δ represents the percentage of the mode diameter shift. N° is the number of analyzed particles.

humidity or availability of reactive gaseous species can also influence the thickness of shell. So, although the present study is limited to specific cases, the data reveal that dependence between the dimensions of Δ_{halo} and d_{core} exists and enable to evaluate a possible range of variability in case of urban and desert aerosol type. The main objective of the study is to parameterize aerosol core-shell structure in remote sensing algorithms. Thus, we should also consider a possible limited sensitivity of optical characteristics to core and shell size dependences. To clarify this question, microscopic observations of core-shell structures from the two described case studies are summarized in a set of parameters and several numerical calculations of aerosol optical characteristics are conducted (see section 3.5).

3.4. Parameterizing Core-Shell Dependencies

The relative contribution of Δ_{halo} to the total particle size (Δ_{halo}/d_{total}), the mean Δ_{halo}, and the corresponding d_{core} can be useful parameters to characterize the core-shell structure. For instance, the ratio Δ_{halo}/d_{total} indicates the fraction of the coating material from the total particle volume. The mean values and the corresponding standard deviations of d_{core}, Δ_{halo}, and Δ_{halo}/d_{total} for all particles and for submicrometer and supermicrometer size fractions, for urban and desert environment cases, are presented in Table 1.

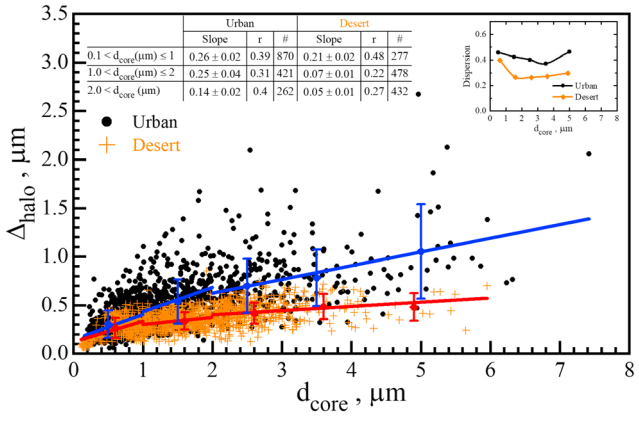

Figure 7. Thickness of halo (Δ_{halo}) versus diameter of particle core (d_{core}) for core-shell particles collected in all size fractions. Black dots and orange crosses correspond to particles collected in urban and desert environment, respectively. The blue and red diamonds with corresponding vertical lines represent the means with standard deviations for three subintervals of d_{core}. Dispersions, calculated as the ratio of Std. Dev. to the mean, are also presented in the insert graph.

In addition, the ratio of Δ_{halo}/d_{total} can be evaluated as a continuous function of the particle size (d_{core}), that is, fitted by an equation, for example, as equation (2):

$$\frac{\Delta_{halo}}{d_{total}} = b + c \cdot \exp(a \cdot d_{core}), \quad (2)$$

whose parameters and coefficient of determination (R^2) for urban and desert particles are reported in Table 2.

The obtained coefficients show that the ratio is higher for small particles in both urban and desert cases. As the diameter of core increases, Δ_{halo}/d_{total} decreases and becomes constant. In the study by Moffet et al. (2016) on black carbon coatings it was also found that smaller particles have thicker shell, which supports the findings in our case studies. In addition, Ibrahim et al. (2018) also showed that smaller mineral dust particles adsorb water more efficiently. It is interesting to note that our finding is also in line with the diffusion growth theory of cloud droplets that states the faster growth for the smaller droplets. That is, although our data present only a snapshot in time, it indicates that the smaller particles grew larger.

3.5. Axis Ratio

Besides the core-shell structure, the particle shape is also known as being important for optical properties of atmospheric aerosols. In addition, since optical properties of core-shell particles are usually modeled by Mie calculations for concentric spheres, a question about the extent of nonsphericity of the observed particles can arise. The particle axis ratio is a parameter that characterizes nonsphericity and it is obtained in this study from the analysis of electron micrographs. Histograms of axis ratio of particles surrounded by halo (core part only, denoted as *particle cores*) and particles without halo (denoted as *not coated particles*) for urban and desert cases are presented in Figure 8. Overall, the range of the axis ratio of particle cores was found to vary from about 1 (spherical particles) to 3. The mean axis ratio of coated cores is 1.37 ± 0.30 (±Standard Deviation) in the case of urban particles and 1.31 ± 0.23 for desert dust particles. Figure 8 shows that coated particles appear more spherical, for both urban and desert cases. These results are in favor of the use of the concentric spheres model for calculations of aerosol optical characteristics.

It should be noted here that, in the case of desert environments, the particles collected in the smallest size fraction were mainly not coated spherical biomass burning particles, which makes the axis ratio of not coated particles to be closer to 1 in desert case. Nevertheless, Figure 8 clearly shows that the presence of coatings shifts the whole histogram of particle cores toward smaller axis ratios, which is true for both urban and desert cases; that is, the coated particles have tendency to be more spherical.

3.6. Optical Properties

The effect of core-shell particle structure on optical properties was evidenced in various studies, either by Mie codes (Lesins et al., 2002; Ramachandran & Srivastava, 2013), or by discrete dipole

Table 1
Mean and Corresponding Standard Deviation of d_{core}, Δ_{halo}, and Δ_{halo}/d_{total} for all Sizes and for Submicrometer and Supermicrometer Size Fractions of d_{core}

	Urban			Desert		
	All sizes (N° = 1,553)	$d_{core} < 1$ μm (N° = 866)	$d_{core} > 1$ μm (N° = 687)	All sizes (N° = 1187)	$d_{core} < 1$ μm (N° = 276)	$d_{core} > 1$ μm (N° = 911)
d_{core} (μm)	1.24 ± 1.00	0.61 ± 0.21	2.03 ± 1.02	1.74 ± 0.92	0.67 ± 0.24	2.06 ± 0.80
Δ_{halo} (μm)	0.45 ± 0.28	0.31 ± 0.14	0.63 ± 0.30	0.35 ± 0.12	0.26 ± 0.11	0.38 ± 0.11
Δ_{halo}/d_{total}	0.22 ± 0.06	0.25 ± 0.05	0.19 ± 0.05	0.16 ± 0.05	0.22 ± 0.05	0.14 ± 0.03

Note. N° denotes the number of particles within each size range.

Table 2
Parameters of Equation (4) and Coefficient of Determination (R^2) for Urban and Desert Particles

	Urban	Desert
b	0.16 ± 0.005	0.09 ± 0.04
c	0.16 ± 0.006	0.21 ± 0.005
a	−1.03 ± 0.01	−0.82 ± 0.05
R^2	0.37	0.65

approximations models (Scarnato et al., 2013; Wu et al., 2016), or by superposition T-Matrix method (Cheng et al., 2014). For sensitivity tests and quantification of coated particle effect on optical properties, some studies assume a shell to core diameter ratio of 2.0 in Cheng et al. (2015), or the shell thickness to core radius ranges from 0.02 to 0.2 in Yin and Liu (2010), or it is calculated from the mass and density of the core and the shell (Ramachandran & Srivastava, 2013). Here we employ the microscopic observations of real airborne particles sampled in urban and desert environments and examine three scenarios of different ways to distribute the thickness of shell on the ensemble of cores. These scenarios are chosen as possible parameterization of the core-shell particles that can be proposed for remote sensing algorithms. We assume that the thickness of halo observed on the substrates is proportional to the real thickness of shell of a coated atmospheric particle. Indeed, the observed halo should be at least in the dimension of cross section of coated particle, however the halo can also be larger due to the impaction during the sampling and to the wettability of the substrate. Therefore, some overestimation of the shell dimension can be possible. At the same time, experience of microscopic observations show that the wetted particles often stay in a liquid form also after the sampling on a substrate; the particles are dried later during the electron micrographs image acquisition, thus we can consider that all particles suffer the same effect in TEM vacuum and during the image acquisition. Given this, and that the wettability of the substrates is the same, it can be expected that the halo dimension is a suitable representation of the shell dimension. Such strategy was used by Moffet et al. (2016) to determine the concentricity between black carbon inclusions particles and their host, where they showed that the majority of black carbon cores are close to the center of their host. In addition, in this work we test the relative dependencies between the shell and core dimensions, rather than using the absolute values of particle dimensions. The coating thickness is represented by the ratio Δ_{shell}/r_{total}, where Δ_{shell} is defined as the difference between the total particle radius and the core radius, that is, the contribution of particle shell thickness to the total particle radius. Thus, the presented above Δ_{halo}/d_{total} is proportional to Δ_{shell}/r_{total} by a factor of two. In this section, we switch from diameters to radii because the aerosol size in remote sensing is commonly described by the radius.

The following computational scenarios are presented: Scenario 1, Δ_{shell}/r_{total} is a continuous function of the total radius (Δ_{shell} is size resolved), as defined by equation (2); Scenario 2, Δ_{shell}/r_{total} is a fixed mean value for all sizes of particles (i.e., 0.44 for urban case and 0.32 for desert case); and Scenario 3, Δ_{shell}/r_{total} is discretized in two mean values, one for fine and one for coarse mode particles, as presented in section 3.4. It should be mentioned that some studies (Bondy, Kirpes, et al., 2017; Grassian & Tivanski, 2018) showed that particles can be also coated by much thin thickness of shell than the ones assumed

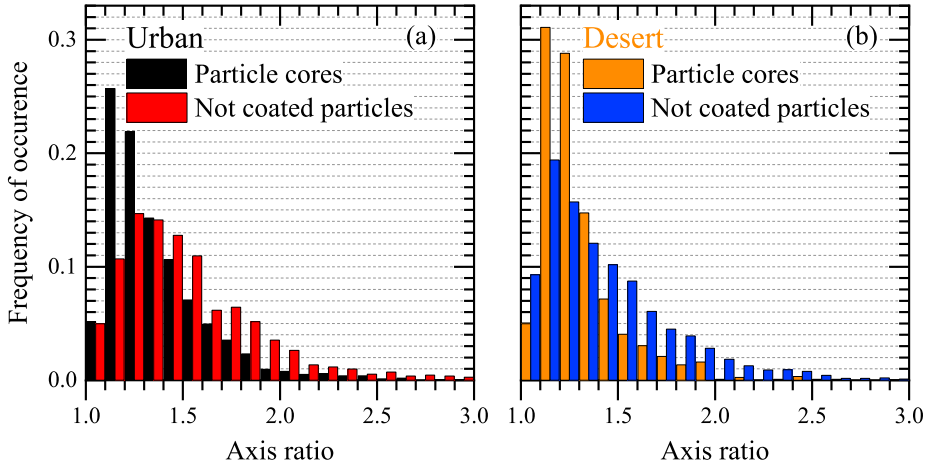

Figure 8. Histograms of axis ratio of particles with halo (core part only, denoted as *particle cores*) and particles without halo (denoted as *not coated particles*) for (a) urban and (b) desert cases.

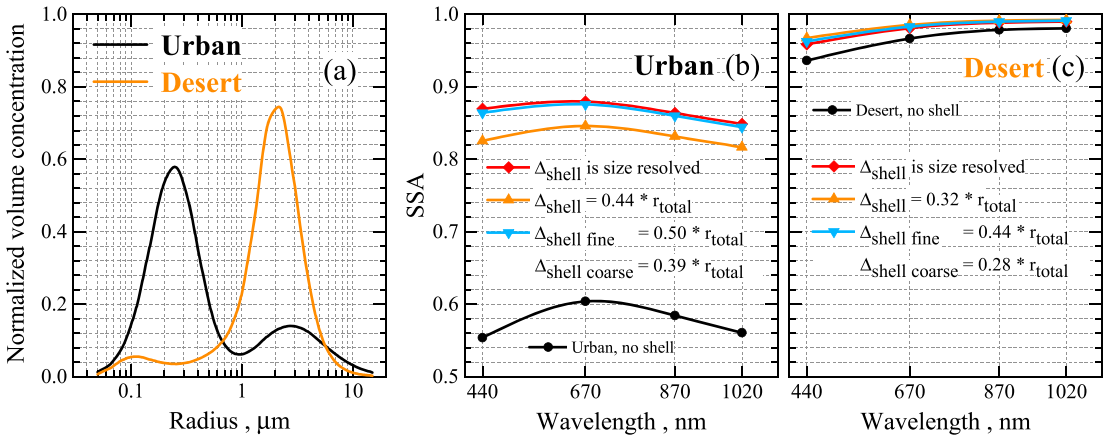

Figure 9. (a) Normalized volume size distributions representative for urban and desert aerosol cases (black and orange curves, respectively). SSA for (b) urban and (c) desert aerosol cases. Black lines represent the SSA of urban and desert aerosols without coating, red lines represent the case with coating where the fraction of Δ_{shell} is a continuous function of particle radius defined by the equation (2), orange lines represent the case where the fraction of Δ_{shell} has same mean value for all particles sizes, blue lines correspond to the case where the fraction of Δ_{shell} is different for the fine and coarse modes and corresponds to the values reported in section 3.4. SSA = single scattering albedo.

in our scenarios. In our work we do not present scenarios with very thin shells because calculations conducted using Δ_{shell}/r_{total} of 0.1 (not shown here) indicated no significant changes in optical properties compared to a homogeneous particle case (i.e., no shell).

To examine the influence of coatings on optical properties of atmospheric particles, we analyzed the changes induced in spectral SSA (ω_0), directional scattering ($P11(\theta, \lambda) \times AOT_{scat}(\lambda)$), and degree of linear polarization ($-P12(\theta, \lambda)/P11(\theta, \lambda)$). We performed tests using the assumption of concentric core-shell particles with volume size distribution typical for urban and desert dust aerosol (Dubovik, Holben, Lapyonok, et al., 2002), as presented in Figure 9a. For the urban environment case, the assumed spectral complex refractive indices (m) is m = 1.59 + 0.172i/1.59 + 0.123i/1.59 + 0.119i/1.59 + 0.119i/at wavelengths 440/670/870/1020 nm, respectively; that represents a volume weighted mixture between 15% of black carbon (m = 1.97 + 0.79i spectrally independent; Bond & Bergstrom, 2006) and 85% of brown carbon (m = 1.54 + 0.0043i/1.54 + 0.0008i/1.54 + 0.0005i/1.54 + 0.0002i at 440/670/870/1020 nm; Dey et al., 2006). In the case of desert particles we used a complex refractive index from Dubovik, Holben, Eck, et al. (2002), Bahrain/Persian Gulf site, which is 1.55 + 0.0025i/0.0014i/0.0010i/0.0010i at 440/670/870/1020 nm, respectively. The coating material is assumed to be nonabsorbing and to be composed of a mixture of ammonium sulfate and water at 90% RH (Table 1 from Erlick et al., 2011) with spectrally independent complex refractive index of $1.37 + 2.084 \times 10^{8}$i, since presence of ultrapure water (real part equal 1.33) is unlikely in the atmosphere. It has to be mentioned that an effect of changing the particle size can be more important than the effect of change in the particle structure (thickness of the coating). Therefore, in the calculations presented here, the volume size distributions are fixed, thus the increase in the thickness of the coating layer is compensated by the proportional decrease of core radius. The comparison of the optical properties is made between coated particles, with the refractive indices for core and shell as previously described, and homogeneous particles with the refractive index of core (denoted as *urban, no shell* and *desert, no shell*).

The SSA (ω_0) is the scattering effectiveness relative to total extinction and is defined as

$$\omega_0 = \frac{\sigma_{sca}}{\sigma_{sca} + \sigma_{abs}}, \tag{3}$$

where σ_{sca} and σ_{abs} are the scattering and absorption coefficients. The spectral directional scattering is described by $P11(\theta, \lambda)$ element of the phase matrix that satisfies the following normalization condition:

$$\frac{1}{2}\int_0^{\pi} P11(\lambda, \theta) \cdot \sin\theta d\theta = 1. \tag{4}$$

The spectral degree of linear polarization is defined as the ratio of $-P12(\theta)$ to $P11(\theta)$ elements of the phase matrix, for single scattering of not polarized incident electromagnetic radiation.

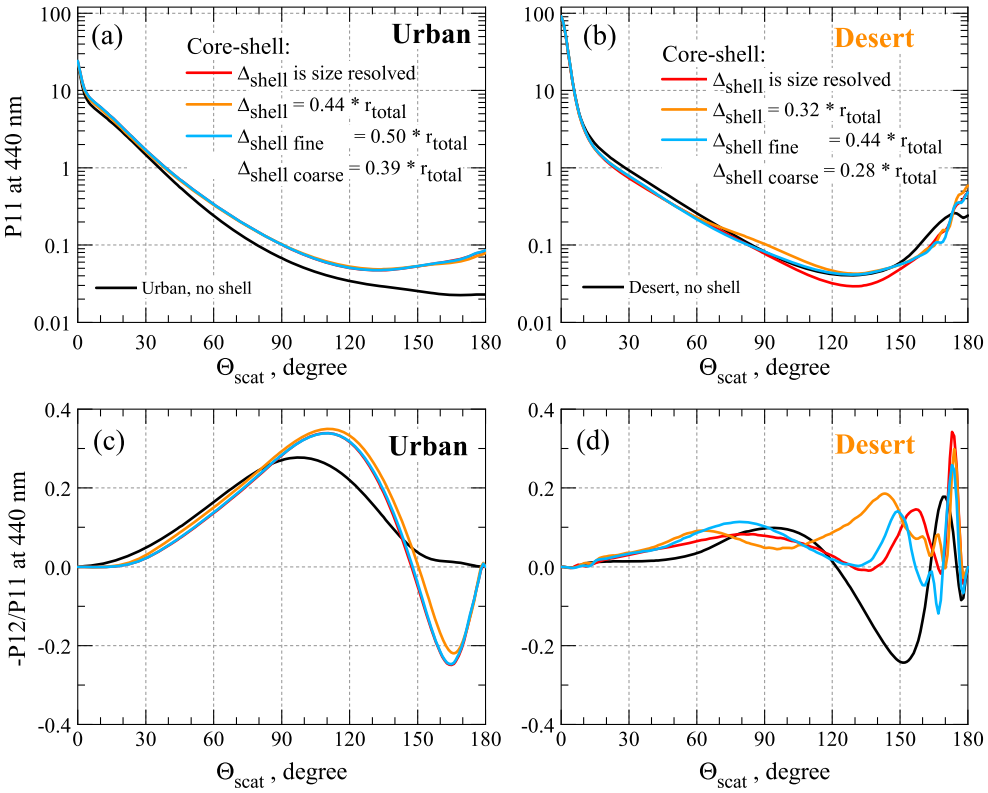

Figure 10. (a), (c) Phase function (P11(θ)) and degree of linear polarization (−P12(θ)/P11(θ)) at 440 nm for the case of urban and (b), (d) of desert environments. The color code description is the same as in Figures 9b and 9c.

In order to conduct the calculations we created a numerical tool that involves the Mie code solving Maxwell's equations for concentric core-shell spheres (Yang et al., 2002), which represents an adaptation of W. Wiscombe's code (Stamnes et al., 1988), and a subroutine for calculating optical characteristics of a polydispersed particle ensemble (Dubovik et al., 2006). The advantage of the Mie modeling is first of all in the computation speed. In general, the randomly oriented spheroids with coating can be used to model aerosol nonsphericity. However, similar to T-Matix for homogeneous spheroids, we expect that the computations will be highly time consuming and there can also be a problem with convergence for the full range of considered sizes and aspect ratios, which is a known problem of the T-Matix code. Computations using other options, for example, the discrete dipole approximation, are even more time consuming and difficult to apply for a realistic range of aerosol sizes. On the other side, the expectation is that the coated particles should be more spherical, as follows from the above analysis in Figure 8. Figure 8 also shows that in the case of urban and desert particles, 53% and 65%, respectively, of the coated particles have the axis ratio between 1 and 1.3. Thus, more than half of the particle cores have nearly spherical shape. Nevertheless, we acknowledge the importance of nonsphericity for optical properties of coated particles, especially because nonsphericity smooths the backward scattering features.

The results of calculations presented in Figure 9b show that when an ensemble of absorbing particle cores is coated by a nonabsorbing shell, ω_0 significantly increases, meaning increasing of scattering effectiveness. The same effect is observed in the case of desert particles, but less pronounced, as illustrated in Figure 9c. Note that the increase in SSA is not contradictory with the absorption enhancement due to the lensing effect, which is defined as the ratio of the σ_{abs} of coated particles to the σ_{abs} of the core only, for example, Fierce et al. (2016). The lensing effect holds for the presented core-shell calculations as well, however, the SSA increases because the increase in σ_{sca} is stronger than the increase in σ_{abs}, for example, in agreement with the results reported by Cheng et al. (2014).

Figure 10a shows that P11(θ) at 440 nm for coated urban particles differs form the homogeneous case, especially in the backscatter direction, however, the way how the thickness of shell is distributed does not

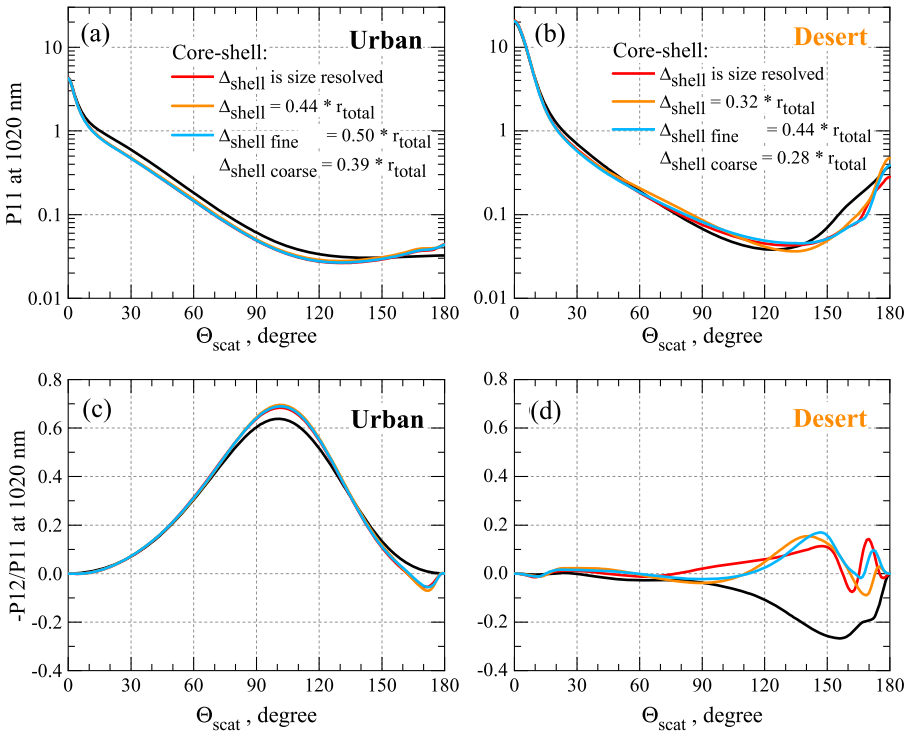

Figure 11. Same as Figure 10, but for 1,020 nm wavelength.

produce an important variability. P11($130° \leq \theta \leq 180°$) at 440 nm for the three scenarios was found higher than for the homogeneous case, for example, by ~50% at $\theta = 130°$ and by ~250% at $\theta = 180°$. The differences in P11(θ) due to how the thickness of shell is distributed become pronounced in the case of coarse mode dominating particles (Figure 10b). In this case, P11($160° \leq \theta \leq 170°$) at 440 nm was found lower than the homogeneous case by ~50%, however, P11($\theta = 180°$) at 440 nm was found higher by ~100% for Scenarios 1 and 3 and by 140% for Scenario 2. Noteworthy, in both cases of fine and coarse mode dominating particles, the differences occur in the backward scattering directions, that can have implications for instruments that mainly measure the backscatter signal, for example, satellite observation of reflected radiation or lidar system. The variability in degree of linear polarization ($-$P12(θ)/P11(θ) at 440 nm) responds much stronger to the shell thickness distribution, for both fine and coarse dominating volume size distributions (Figures 10c and 10d). $-$P12(θ)/P11(θ) at 440 nm also presents a much stronger difference versus the homogeneous scenario, both for desert and urban cases. The differences are distinguishable in side and backward scattering directions. In the case of fine mode dominating particles, the scenario when Δ_{shell}/r_{total} is fixed for all sizes (Scenario 2) is only slightly distinguishable from the rest of the scenarios. However, the differences in $-$P12(θ)/P11(θ) becomes much more important in the case of coarse mode dominating particles; all three scenarios give noticeable differences in this case.

It can be expected that the effect of the coating and the way how the shell thickness is distributed on the ensemble of cores will be manifested differently at different wavelengths. In order to examine the spectral dependence of optical characteristics, the phase function and degree of linear polarization at 1,020 nm are presented in Figure 11. In the case of fine and coarse mode dominating particles, P11(θ) and $-$P12(θ)/P11(θ) at 1,020 nm exert sensitivity to the appearance of coatings versus homogeneous particles, that is, the differences appear in side and backward scattering directions, similar to 440 nm. However, the influence of Δ_{shell}/r_{total} distribution is diminished with increase of the wavelength. In fact, an increase of the wavelength in this case can be equivalent to a decrease of the coating dimension.

Significance of the differences in the phase function and the degree of linear polarization due to the coating merits a separate study, dedicated to evaluating the effect on the aerosol microphysical characteristics retrievals. It should be tested for different levels of noise and involving multiple scattering. Meanwhile, a

preliminary assessment of the difference, obtained under single scattering approximation, shows that the effects can be comparable with those of particle nonsphericity or varying complex refractive index, for example, Figures 27 to 30 in Dubovik et al. (2006).

4. Summary and Conclusions

The individual particle analysis presented in this work shows that, during an urban pollution event in northern France, the majority of particles sampled had a coating. The coating was also found on airborne particles sampled at altitude of 3.7 km in desert environment of western Africa. Possibility of coating of anthropogenic and dust particles is in agreement with a number of previous laboratory and field works (Dentener et al., 1996; Falkovich et al., 2004; Krueger, 2003; Krueger et al., 2004; Laskin et al., 2005; Zuberi et al., 2005). The main goals of the presented study consisted in a statistical analysis of collected particle core and shell dimensions derived from microscopic observations and in finding relationships between them for a possible parameterization in remote sensing applications. It was found that in urban environment during an elevated pollution event, the coated particles outnumbered (60% of 2,569 analyzed particles) the not coated ones. In the desert environment, the coated particles represented 20% of 5,872 analyzed particles. It was found that the size of the halo generally increases with the size of the core, however, the increase is steeper for smaller particles. The ratio of halo thickness to total particle diameter was evaluated for different size fractions. The relative contribution of the halo thickness to the total particle diameter was found to be more important for the smaller particles. Assuming that the dimensions of halo are representative for the dimensions of the particle shell, the obtained results served for parameterizing different scenarios of the shell thickness distribution. The changes in calculated aerosol optical properties due to different ways of parameterization were examined. A series of calculations for the urban and desert aerosol types revealed that despite a pronounced difference between presence and absence of shell, the variability in aerosol optical characteristics due to different ways to parameterize the dimensions of shell is quite weak in the case of fine mode dominating particles. However, in the case of coarse mode dominating particles, the way to represent the thickness of shell becomes important. Generally, the scattering in side and backward directions is most sensitive to the presence of coating and to the different representations of shell dimensions. The degree of linear polarization appears as the most sensitive to the presence of the core-shell structure, the variability in its dimensions, and the way to parameterize it. In support of the use of a spherical particle model for calculations of core-shell aerosol optical characteristics, it was found that the axis ratios of coated cores are shifted toward smaller values as compared to not coated particles; this fact indicates that the particles that experienced coating tend to be more spherical.

Because one of the difficulties is to quantify the complex aerosol morphology by a reasonable number of parameters, the obtained information can be particularly valuable for parameterization of atmospheric aerosol core-shell structure and implementation in advanced remote sensing algorithms.

Acknowledgments
The work is supported by the CaPPA project. The CaPPA project (Chemical and Physical Properties of the Atmosphere) is funded by the French National Research Agency (ANR) through the PIA (Programme d'Investissement d'Avenir) under contract "ANR-11-LABX-0005-01" and by the Regional Council "Hauts-de-France" and the "European Funds for Regional Economic Development" (FEDER). Authors would like to thank also to ATMO-Hauts-de-France for providing the $PM_{10,\ 2.5}$ data. All the data used are listed in the references or archived in repositories as following: The AERONET data are available at https://aeronet.gsfc.nasa.gov/index.html. The extinction profiles, meteorological parameters, and PM's concentrations are available at http://www-loa.univ-lille1.fr/observations/sites_instru.html, http://www.atmo-hdf.fr. TEM images, core/shell dimensions, aspect ratio of investigated particles, and results of the simulations, are available at https://doi.org/10.17605/OSF.IO/3NZB5.

References

Adachi, K., & Buseck, P. R. (2013). Changes of ns-soot mixing states and shapes in an urban area during CalNex. *Journal of Geophysical Research: Atmospheres*, *118*, 3723–3730. https://doi.org/10.1002/jgrd.50321

Adachi, K., Chung, S. H., & Buseck, P. R. (2010). Shapes of soot aerosol particles and implications for their effects on climate. *Journal of Geophysical Research*, *115*, D15206. https://doi.org/10.1029/2009JD012868

Bauer, S. E., Mishchenko, M. I., Lacis, A. A., Zhang, S., Perlwitz, J., & Metzger, S. M. (2007). Do sulfate and nitrate coatings on mineral dust have important effects on radiative properties and climate modeling? *Journal of Geophysical Research*, *112*, D06307. https://doi.org/10.1029/2005JD006977

Bescond, A., Yon, J., Ouf, F. X., Ferry, D., Delhaye, D., Gaffié, D., et al. (2014). Automated determination of aggregate primary particle size distribution by tem image analysis: Application to soot. *Aerosol Science and Technology*, *48*(8), 831–841. https://doi.org/10.1080/02786826.2014.932896

Bond, T. C., & Bergstrom, R. W. (2006). Light absorption by carbonaceous particles: An investigative review. *Aerosol Science and Technology*, *40*(1), 27–67. https://doi.org/10.1080/02786820500421521

Bond, T. C., Habib, G., & Bergstrom, R. W. (2006). Limitations in the enhancement of visible light absorption due to mixing state. *Journal of Geophysical Research*, *111*, D20211. https://doi.org/10.1029/2006JD007315

Bondy, A. L., Kirpes, R. M., Merzel, R. L., Pratt, K. A., Banaszak Holl, M. M., & Ault, A. P. (2017). Atomic force microscopy-infrared spectroscopy of individual atmospheric aerosol particles: Subdiffraction limit vibrational spectroscopy and morphological analysis. *Analytical Chemistry*, *89*(17), 8594–8598. https://doi.org/10.1021/acs.analchem.7b02381

Bondy, A. L., Wang, B., Laskin, A., Craig, R. L., Nhliziyo, M. V., Bertman, S. B., et al. (2017). Inland sea spray aerosol transport and incomplete chloride depletion: Varying degrees of reactive processing observed during SOAS. *Environmental Science and Technology*, *51*(17), 9533–9542. https://doi.org/10.1021/acs.est.7b02085

Bovchaliuk, V., Goloub, P., Podvin, T., Veselovskii, I., Tanre, D., Chaikovsky, A., et al. (2016). Comparison of aerosol properties retrieved using GARRLiC, LIRIC, and Raman algorithms applied to multi-wavelength lidar and sun/sky-photometer data. *Atmospheric Measurement Techniques*, *9*(7), 3391–3405. https://doi.org/10.5194/amt-9-3391-2016

Cappa, C. D., Onasch, T. B., Massoli, P., Worsnop, D. R., Bates, T. S., Cross, E. S., et al. (2012). Radiative absorption enhancements due to the mixing state of atmospheric black carbon. *Science*, *337*(6098), 1078–1081. https://doi.org/10.1126/science.1223447

Chakrabarty, R. K., Moosmüller, H., Chen, L. W. A., Lewis, K., Arnott, W. P., Mazzoleni, C., et al. (2010). Brown carbon in tar balls from smoldering biomass combustion. *Atmospheric Chemistry and Physics*, *10*(13), 6363–6370. https://doi.org/10.5194/acp-10-6363-2010

Cheng, T., Gu, X., Wu, Y., & Chen, H. (2014). Effects of atmospheric water on the optical properties of soot aerosols with different mixing states. *Journal of Quantitative Spectroscopy and Radiative Transfer*, *147*, 196–206. https://doi.org/10.1016/j.jqsrt.2014.06.002

Cheng, T., Wu, Y., Gu, X., & Chen, H. (2015). Effects of mixing states on the multiple-scattering properties of soot aerosols. *Optics Express*, *23*(8), 10,808–10,821. https://doi.org/10.1364/OE.23.010808

China, S., Mazzoleni, C., Gorkowski, K., Aiken, A. C., & Dubey, M. K. (2013). Morphology and mixing state of individual freshly emitted wildfire carbonaceous particles. *Nature Communications*, *4*(1), 2122. https://doi.org/10.1038/ncomms3122

Choël, M., Deboudt, K., Flament, P., Aimoz, L., & Mériaux, X. (2007). Single-particle analysis of atmospheric aerosols at Cape Gris-Nez, English Channel: Influence of steel works on iron apportionment. *Atmospheric Environment*, *41*(13), 2820–2830. https://doi.org/10.1016/j.atmosenv.2006.11.038

Chou, C., Formenti, P., Maille, M., Ausset, P., Helas, G., Harrison, M., & Osborne, S. (2008). Size distribution, shape, and composition of mineral dust aerosols collected during the African monsoon multidisciplinary analysis special observation period 0: Dust and biomass-burning experiment field campaign in Niger, January 2006. *Journal of Geophysical Research*, *113*, D00C10. https://doi.org/10.1029/2008JD009897

Deboudt, K., Flament, P., Choël, M., Gloter, A., Sobanska, S., & Colliex, C. (2010). Mixing state of aerosols and direct observation of carbonaceous and marine coatings on African dust by individual particle analysis. *Journal of Geophysical Research*, *115*, D24207. https://doi.org/10.1029/2010JD013921

Dentener, F. J., Carmichael, G. R., Zhang, Y., Lelieveld, J., & Crutzen, P. J. (1996). Role of mineral aerosol as a reactive surface in the global troposphere. *Journal of Geophysical Research*, *101*(D17), 22,869–22,889. https://doi.org/10.1029/96JD01818

Derimian, Y., Choël, M., Rudich, Y., Deboudt, K., Dubovik, O., Laskin, A., et al. (2017). Effect of sea breeze circulation on aerosol mixing state and radiative properties in a desert setting. *Atmospheric Chemistry and Physics*, *17*(18), 11,331–11,353. https://doi.org/10.5194/acp-17-11331-2017

Dey, S., Tripathi, S. N., Singh, R. P., & Holben, B. N. (2006). Retrieval of black carbon and specific absorption over Kanpur city, northern India during 2001–2003 using AERONET data. *Atmospheric Environment*, *40*(3), 445–456. https://doi.org/10.1016/j.atmosenv.2005.09.053

Dubovik, O., Holben, B., Eck, T. F., Smirnov, A., Kaufman, Y. J., King, M. D., et al. (2002). Variability of absorption and optical properties of key aerosol types observed in worldwide locations. *Journal of the Atmospheric Sciences*, *59*(3), 590–608. https://doi.org/10.1175/1520-0469(2002)059<0590:VOAAOP>2.0.CO;2

Dubovik, O., Holben, B. N., Lapyonok, T., Sinyuk, A., Mishchenko, M. I., Yang, P., & Slutsker, I. (2002). Non-spherical aerosol retrieval method employing light scattering by spheroids. *Geophysical Research Letters*, *29*(10), 1415. https://doi.org/10.1029/2001GL014506

Dubovik, O., Sinyuk, A., Lapyonok, T., Holben, B. N., Mishchenko, M., Yang, P., et al. (2006). Application of spheroid models to account for aerosol particle nonsphericity in remote sensing of desert dust. *Journal of Geophysical Research*, *111*, D11208. https://doi.org/10.1029/2005JD006619

Easter, R. C., Ghan, S. J., Zhang, Y., Saylor, R. D., Chapman, E. G., Laulainen, N. S., et al. (2004). MIRAGE: Model description and evaluation of aerosols and trace gases. *Journal of Geophysical Research*, *109*(D20), D20210. https://doi.org/10.1029/2004JD004571

Eck, T. F., Holben, B. N., Reid, J. S., Dubovik, O., Smirnov, A., O'Neill, N. T., et al. (1999). Wavelength dependence of the optical depth of biomass burning, urban, and desert dust aerosols. *Journal of Geophysical Research*, *104*(D24), 31,333–31,349. https://doi.org/10.1029/1999JD900923

Elliot, A. J., Smith, S., Dobney, A., Thornes, J., Smith, G. E., & Vardoulakis, S. (2016). Monitoring the effect of air pollution episodes on health care consultations and ambulance call-outs in England during March/April 2014: A retrospective observational analysis. *Environmental Pollution*, *214*, 903–911. https://doi.org/10.1016/j.envpol.2016.04.026

Engelhart, G. J., Hildebrandt, L., Kostenidou, E., Mihalopoulos, N., Donahue, N. M., & Pandis, S. N. (2011). Water content of aged aerosol. *Atmospheric Chemistry and Physics*, *11*(3), 911–920. https://doi.org/10.5194/acp-11-911-2011

Erlick, C., Abbatt, J. P. D., & Rudich, Y. (2011). How different calculations of the refractive index affect estimates of the radiative forcing efficiency of ammonium sulfate aerosols. *Journal of the Atmospheric Sciences*, *68*(9), 1845–1852. https://doi.org/10.1175/2011JAS3721.1

Falkovich, A. H., Schkolnik, G., Ganor, E., & Rudich, Y. (2004). Adsorption of organic compounds pertinent to urban environments onto mineral dust particles. *Journal of Geophysical Research*, *109*, D02208. https://doi.org/10.1029/2003JD003919

Fan, J., Shao, L., Hu, Y., Wang, J., Wang, J., & Ma, J. (2016). Classification and chemical compositions of individual particles at an eastern marginal site of Tibetan Plateau. *Atmospheric Pollution Research*, *7*(5), 833–842. https://doi.org/10.1016/j.apr.2016.04.007

Fard, M. M., Krieger, U. K., & Peter, T. (2017). Kinetic limitation to inorganic ion diffusivity and to coalescence of inorganic inclusions in viscous liquid-liquid phase-separated particles. *Journal of Physical Chemistry A*, *121*(48), 9284–9296. https://doi.org/10.1021/acs.jpca.7b05242

Fierce, L., Bond, T. C., Bauer, S. E., Mena, F., & Riemer, N. (2016). Black carbon absorption at the global scale is affected by particle-scale diversity in composition. *Nature Communications*, *7*, 12361. https://doi.org/10.1038/ncomms12361

Flament, P., Deboudt, K., Cachier, H., Châtenet, B., & Mériaux, X. (2011). Mineral dust and carbonaceous aerosols in West Africa: Source assessment and characterization. *Atmospheric Environment*, *45*(22), 3742–3749. https://doi.org/10.1016/j.atmosenv.2011.04.013

Fuller, K. A. (1995). Scattering and absorption cross sections of compounded spheres. II. Calculations for external aggregation. *Journal of the Optical Society of America A*, *12*(5), 881–892. https://doi.org/10.1364/JOSAA.12.000881

Fuller, K. A., & Kreidenweis, S. M. (1999). Effects of mixing on extinction by carbonaceous particles. *Journal of Geophysical Research*, *104*(D13), 15,941–15,954. https://doi.org/10.1029/1998JD100069

Grassian, V. H., & Tivanski, A. V. (2018). Lab on a tip: Atomic force microscopy – Photothermal infrared spectroscopy of atmospherically relevant organic/inorganic aerosol particles in the nanometer to micrometer size range. *The Analyst*, *143*(12), 2765–2774. https://doi.org/10.6075/J0F47MBF

Hamacher-Barth, E., Jansson, K., & Leck, C. (2013). A method for sizing submicrometer particles in air collected on Formvar films and imaged by scanning electron microscope. *Atmospheric Measurement Techniques*, *6*(12), 3459–3475. https://doi.org/10.5194/amt-6-3459-2013

Hamacher-Barth, E., Leck, C., & Jansson, K. (2016). Size-resolved morphological properties of the high Arctic summer aerosol during ASCOS-2008. *Atmospheric Chemistry and Physics*, *16*(10), 6577–6593. https://doi.org/10.5194/acp-16-6577-2016

Hand, V. L., Capes, G., Vaughan, D. J., Formenti, P., Haywood, J. M., & Coe, H. (2010). Evidence of internal mixing of African dust and biomass burning particles by individual particle analysis using electron beam techniques. *Journal of Geophysical Research*, *115*, D13301. https://doi.org/10.1029/2009JD012938

Haywood, J. M., Pelon, J., Formenti, P., Bharmal, N. A., Brooks, M. E., Capes, G., et al. (2008). Overview of the dust and biomass-burning experiment and African monsoon multidisciplinary analysis special observing period-0. *Journal of Geophysical Research*, *113*, D00C17. https://doi.org/10.1029/2008JD010077

Healy, R. M., Sciare, J., Poulain, L., Crippa, M., Wiedensohler, A., Prévôt, A. S. H., et al. (2013). Quantitative determination of carbonaceous particle mixing state in Paris using single-particle mass spectrometer and aerosol mass spectrometer measurements. *Atmospheric Chemistry and Physics*, *13*(18), 9479–9496. https://doi.org/10.5194/acp-13-9479-2013

Hoflich, B. L. W., Weinbruch, S., Theissmann, R., Gorzawski, H., Ebert, M., Ortner, H. M., et al. (2005). Characterization of individual aerosol particles workroom air of aluminium smelter potrooms. *Journal of Environmental Monitoring*, *7*(5), 419–424. https://doi.org/10.1039/b418275h

Holben, B. N., Eck, T. F., Slutsker, I., Tanré, D., Buis, J. P., Setzer, A., et al. (1998). AERONET—A federated instrument network and data archive for aerosol characterization. *Remote Sensing of Environment*, *66*(1), 1–16. https://doi.org/10.1016/S0034-4257(98)00031-5

Huffman, J. A., Sinha, B., Garland, R. M., Snee-Pollmann, A., Gunthe, S. S., Artaxo, P., et al. (2012). Size distributions and temporal variations of biological aerosol particles in the Amazon rainforest characterized by microscopy and real-time UV-APS fluorescence techniques during AMAZE-08. *Atmospheric Chemistry and Physics*, *12*(24), 11,997–12,019. https://doi.org/10.5194/acp-12-11997-2012

Hwang, H. J., & Ro, C. U. (2006). Direct observation of nitrate and sulfate formations from mineral dust and sea-salts using low-Z particle electron probe X-ray microanalysis. *Atmospheric Environment*, *40*(21), 3869–3880. https://doi.org/10.1016/j.atmosenv.2006.02.022

Ibrahim, S., Romanias, M. N., Alleman, L. Y., Zeineddine, M. N., Angeli, G. K., Trikalitis, P. N., & Thevenet, F. (2018). Water interaction with mineral dust aerosol: Particle size and hygroscopic properties of dust. *ACS Earth and Space Chemistry*, *2*(4), 376–386. https://doi.org/10.1021/acsearthspacechem.7b00152

Johnson, K. S., Zuberi, B., Molina, L. T., Molina, M. J., Iedema, M. J., Cowin, J. P., et al. (2005). Processing of soot in an urban environment: Case study from the Mexico City Metropolitan Area. *Atmospheric Chemistry and Physics*, *5*, 3033–3043. https://doi.org/10.5194/acp-5-3033-2005

Kahnert, M. (2015). Modelling radiometric properties of inhomogeneous mineral dust particles: Applicability and limitations of effective medium theories. *Journal of Quantitative Spectroscopy and Radiative Transfer*, *152*, 16–27. https://doi.org/10.1016/j.jqsrt.2014.10.025

Kandler, K., Benker, N., Bundke, U., Cuevas, E., Ebert, M., Knippertz, P., et al. (2007). Chemical composition and complex refractive index of Saharan Mineral Dust at Izaña, Tenerife (Spain) derived by electron microscopy. *Atmospheric Environment*, *41*(37), 8058–8074. https://doi.org/10.1016/j.atmosenv.2007.06.047

Khalizov, A. F., Zhang, R., Zhang, D., Xue, H., Pagels, J., & McMurry, P. H. (2009). Formation of highly hygroscopic soot aerosols upon internal mixing with sulfuric acid vapor. *Journal of Geophysical Research*, *114*, D05208. https://doi.org/10.1029/2008JD010595

Kojima, T., Buseck, P. R., Iwasaka, Y., Matsuki, A., & Trochkine, D. (2006). Sulfate-coated dust particles in the free troposphere over Japan. *Atmospheric Research*, *82*(3–4), 698–708. https://doi.org/10.1016/j.atmosres.2006.02.024

Kreidenweis, S. M., Petters, M. D., & Demott, P. J. (2008). Single-parameter estimates of aerosol water content. *Environmental Research Letters*, *3*(3). https://doi.org/10.1088/1748-9326/3/3/035002

Krueger, B. J. (2003). The transformation of solid atmospheric particles into liquid droplets through heterogeneous chemistry: Laboratory insights into the processing of calcium containing mineral dust aerosol in the troposphere. *Geophysical Research Letters*, *30*(3), 1148. https://doi.org/10.1029/2002GL016563

Krueger, B. J., Grassian, V. H., Cowin, J. P., & Laskin, A. (2004). Heterogeneous chemistry of individual mineral dust particles from different dust source regions: The importance of particle mineralogy. *Atmospheric Environment*, *38*(36), 6253–6261. https://doi.org/10.1016/j.atmosenv.2004.07.010

Lang-Yona, N., Abo-Riziq, A., Erlick, C., Segre, E., Trainic, M., & Rudich, Y. (2010). Interaction of internally mixed aerosols with light. *Physical Chemistry Chemical Physics*, *12*(1), 21–31. https://doi.org/10.1039/B913176K

Laskin, A., Cowin, J. P., & Iedema, M. J. (2006). Analysis of individual environmental particles using modern methods of electron microscopy and X-ray microanalysis. *Journal of Electron Spectroscopy and Related Phenomena*, *150*(2–3), 260–274. https://doi.org/10.1016/j.elspec.2005.06.008

Laskin, A., Gilles, M. K., Knopf, D. A., Wang, B., & China, S. (2016). Progress in the analysis of complex atmospheric particles. *Annual Review of Analytical Chemistry*, *9*(1), 117–143. https://doi.org/10.1146/annurev-anchem-071015-041521

Laskin, A., Iedema, M. J., Ichkovich, A., Graber, E. R., Taraniuk, I., & Rudich, Y. (2005). Direct observation of completely processed calcium carbonate dust particles. *Faraday Discussions*, *130*, 453. https://doi.org/10.1039/b417366j

Laskina, O., Morris, H. S., Grandquist, J. R., Qin, Z., Stone, E. A., Tivanski, A. V., & Grassian, V. H. (2015). Size matters in the water uptake and hygroscopic growth of atmospherically relevant multicomponent aerosol particles. *Journal of Physical Chemistry A*, *119*(19), 4489–4497. https://doi.org/10.1021/jp510268p

Laskina, O., Young, M. A., Kleiber, P. D., & Grassian, V. H. (2013). Infrared extinction spectroscopy and micro-Raman spectroscopy of select components of mineral dust mixed with organic compounds. *Journal of Geophysical Research: Atmospheres*, *118*, 6593–6606. https://doi.org/10.1002/jgrd.50494

Léon, J. F., Derimian, Y., Chiapello, I., Tanré, D., Podvin, T., Chatenet, B., et al. (2009). Aerosol vertical distribution and optical properties over M'Bour (16.96° W; 14.39° N), Senegal from 2006 to 2008. *Atmospheric Chemistry and Physics*, *9*(23), 9249–9261. https://doi.org/10.5194/acp-9-9249-2009

Lesins, G., Chylek, P., & Lohmann, U. (2002). A study of internal and external mixing scenarios and its effect on aerosol optical properties and direct radiative forcing. *Journal of Geophysical Research*, *107*(D10), 4094. https://doi.org/10.1029/2001JD000973

Li, W., & Shao, L. (2009a). Transmission electron microscopy study of aerosol particles from the brown hazes in northern China. *Journal of Geophysical Research*, *114*, D09302. https://doi.org/10.1029/2008JD011285

Li, W. J., & Shao, L. Y. (2009b). Observation of nitrate coatings on atmospheric mineral dust particles. *Atmospheric Chemistry and Physics*, *9*(6), 1863–1871. https://doi.org/10.5194/acp-9-1863-2009

Li, W. J., Zhang, D. Z., Shao, L. Y., Zhou, S. Z., & Wang, W. X. (2011). Individual particle analysis of aerosols collected under haze and non-haze conditions at a high-elevation mountain site in the North China plain. *Atmospheric Chemistry and Physics*, *11*(22), 11,733–11,744. https://doi.org/10.5194/acp-11-11733-2011

Li, Z., Gu, X., Wang, L., Li, D., Xie, Y., Li, K., et al. (2013). Aerosol physical and chemical properties retrieved from ground-based remote sensing measurements during heavy haze days in Beijing winter. *Atmospheric Chemistry and Physics*, *13*(20), 10,171–10,183. https://doi.org/10.5194/acp-13-10171-2013

Liu, C., Panetta, R. L., & Yang, P. (2014). Inhomogeneity structure and the applicability of effective medium approximations in calculating light scattering by inhomogeneous particles. *Journal of Quantitative Spectroscopy and Radiative Transfer*, *146*, 331–348. https://doi.org/10.1016/j.jqsrt.2014.03.018

Macintyre, H. L., Heaviside, C., Neal, L. S., Agnew, P., Thornes, J., & Vardoulakis, S. (2016). Mortality and emergency hospitalizations associated with atmospheric particulate matter episodes across the UK in spring 2014. *Environment International*, *97*, 108–116. https://doi.org/10.1016/j.envint.2016.07.018

Marris, H., Deboudt, K., Flament, P., Grobéty, B., & Gieré, R. (2013). Fe and Mn oxidation states by TEM-EELS in fine-particle emissions from a Fe-Mn alloy making plant. *Environmental Science and Technology*, *47*(19), 10,832–10,840. https://doi.org/10.1021/es400368s

Matsuki, A., Iwasaka, Y., Shi, G., Zhang, D., Trochkine, D., Yamada, M., et al. (2005). Morphological and chemical modification of mineral dust: Observational insight into the heterogeneous uptake of acidic gases. *Geophysical Research Letters*, *32*, L22806. https://doi.org/10.1029/2005GL024176

Mikhailov, E. F., Mironov, G. N., Pöhlker, C., Chi, X., Krüger, M. L., Shiraiwa, M., et al. (2015). Chemical composition, microstructure, and hygroscopic properties of aerosol particles at the Zotino Tall Tower Observatory (ZOTTO), Siberia, during a summer campaign. *Atmospheric Chemistry and Physics*, *15*(15), 8847–8869. https://doi.org/10.5194/acp-15-8847-2015

Mishchenko, M. I., Liu, L., Cairns, B., & Mackowski, D. W. (2014). Optics of water cloud droplets mixed with black-carbon aerosols. *Optics Letters*, *39*(9), 2607–2610. https://doi.org/10.1364/OL.39.002607

Mishchenko, M. I., & Travis, L. D. (1994). Light scattering by polydispersions of randomly oriented spheroids with sizes comparable to wavelengths of observation. *Applied Optics*, *33*(30), 7206–7225. https://doi.org/10.1364/AO.33.007206

Moffet, R. C., Henn, T. R., Tivanski, A. V., Hopkins, R. J., Desyaterik, Y., Kilcoyne, A. L. D., et al. (2010). Microscopic characterization of carbonaceous aerosol particle aging in the outflow from Mexico City. *Atmospheric Chemistry and Physics*, *10*(3), 961–976. https://doi.org/10.5194/acp-10-961-2010

Moffet, R. C., O'Brien, R. E., Alpert, P. A., Kelly, S. T., Pham, D. Q., Gilles, M. K., et al. (2016). Morphology and mixing of black carbon particles collected in Central California during the CARES field study. *Atmospheric Chemistry and Physics*, *16*(22), 14,515–14,525. https://doi.org/10.5194/acp-16-14515-2016

Mortier, A., Goloub, P., Derimian, Y., Tanré, D., Podvin, T., Blarel, L., et al. (2016). Climatology of aerosol properties and clear-sky shortwave radiative effects using lidar and sun photometer observations in the Dakar site. *Journal of Geophysical Research: Atmospheres*, *121*, 6489–6510. https://doi.org/10.1002/2015JD024588

Mortier, A., Goloub, P., Podvin, T., Deroo, C., Chaikovsky, A., Ajtai, N., et al. (2013). Detection and characterization of volcanic ash plumes over Lille during the Eyjafjallajökull eruption. *Atmospheric Chemistry and Physics*, *13*(7), 3705–3720. https://doi.org/10.5194/acp-13-3705-2013

Müller, A., Miyazaki, Y., Aggarwal, S. G., Kitamori, Y., Boreddy, S. K. R., & Kawamura, K. (2017). Effects of chemical composition and mixing state on size-resolved hygroscopicity and cloud condensation nuclei activity of submicron aerosols at a suburban site in northern Japan in summer. *Journal of Geophysical Research: Atmospheres*, *122*, 9301–9318. https://doi.org/10.1002/2017JD027286

Nguyen, T. K. V., Zhang, Q., Jimenez, J. L., Pike, M., & Carlton, A. G. (2016). Liquid water: Ubiquitous contributor to aerosol mass. *Environmental Science & Technology Letters*, *3*(7), 257–263. https://doi.org/10.1021/acs.estlett.6b00167

Niemi, J. V., Saarikoski, S., Tervahattu, H., Mäkelä, T., Hillamo, R., Vehkamäki, H., et al. (2006). Changes in background aerosol composition in Finland during polluted and clean periods studied by TEM/EDX individual particle analysis. *Atmospheric Chemistry and Physics*, *6*(12), 5049–5066. https://doi.org/10.5194/acp-6-5049-2006

Niu, H., Hu, W., Pian, W., Fan, J., & Wang, J. (2015). Evolution of atmospheric aerosol particles during a pollution accumulation process: A case study. *World Journal of Engineering*, *12*(1), 51–60. https://doi.org/10.1260/1708-5284.12.1.51

Osborne, S. R., Johnson, B. T., Haywood, J. M., Baran, A. J., Harrison, M. A. J., & McConnell, C. L. (2008). Physical and optical properties of mineral dust aerosol during the dust and biomass-burning experiment. *Journal of Geophysical Research*, *113*, D00C03. https://doi.org/10.1029/2007JD009551

Péré, J. C., Rivellini, L., Crumeyrolle, S., Chiapello, I., Minvielle, F., Thieuleux, F., et al. (2018). Simulation of African dust properties and radiative effects during the 2015 SHADOW campaign in Senegal. *Atmospheric Research*, *199*, 14–28. https://doi.org/10.1016/j.atmosres.2017.07.027

Pirjola, L., Niemi, J. V., Saarikoski, S., Aurela, M., Enroth, J., Carbone, S., et al. (2017). Physical and chemical characterization of urban wintertime aerosols by mobile measurements in Helsinki, Finland. *Atmospheric Environment*, *158*, 60–75. https://doi.org/10.1016/j.atmosenv.2017.03.028

Pósfai, M., Axisa, D., Tompa, É., Freney, E., Bruintjes, R., & Buseck, P. R. (2013). Interactions of mineral dust with pollution and clouds: An individual-particle TEM study of atmospheric aerosol from Saudi Arabia. *Atmospheric Research*, *122*, 347–361. https://doi.org/10.1016/j.atmosres.2012.12.001

Pósfai, M., & Buseck, P. R. (2010). Nature and climate effects of individual tropospheric aerosol particles. *Annual Review of Earth and Planetary Sciences*, *38*(1), 17–43. https://doi.org/10.1146/annurev.earth.031208.100032

Pósfai, M., Simonics, R., Li, J., Hobbs, P. V., & Buseck, P. R. (2003). Individual aerosol particles from biomass burning in southern Africa: 1. Compositions and size distributions of carbonaceous particles. *Journal of Geophysical Research*, *108*(D13), 8483. https://doi.org/10.1029/2002JD002291

Pósfai, M., Xu, H., Anderson, J. R., & Buseck, P. R. (1998). Wet and dry sizes of atmospheric aerosol particles: An AFM-TEM Study. *Geophysical Research Letters*, *25*(11), 1907–1910. https://doi.org/10.1029/98GL01416

Ramachandran, S., & Srivastava, R. (2013). Influences of external vs. core–shell mixing on aerosol optical properties at various relative humidities. *Environmental Science: Processes & Impacts*, *15*(5), 1070–1077. https://doi.org/10.1039/c3em30975d

Reid, J. S., Eck, T. F., Christopher, S. A., Koppmann, R., Dubovik, O., Eleuterio, D. P., et al. (2005). A review of biomass burning emissions part III: Intensive optical properties of biomass burning particles. *Atmospheric Chemistry and Physics*, *5*, 827–849. https://doi.org/10.5194/acp-5-827-2005

Reid, J. S., Koppmann, R., Eck, T. F., & Eleuterio, D. P. (2005). A review of biomass burning emissions part II: Intensive physical properties of biomass burning particles. *Atmospheric Chemistry and Physics*, *5*(3), 799–825. https://doi.org/10.5194/acp-5-799-2005

Rivellini, L. H., Chiapello, I., Tison, E., Fourmentin, M., Feron, A., Diallo, A., et al. (2017). Chemical characterization and source apportionment of submicron aerosols measured in Senegal during the 2015 SHADOW campaign. *Atmospheric Chemistry and Physics*, *17*(17), 10,291–10,314. https://doi.org/10.5194/acp-17-10291-2017

Rocha-Lima, A., Martins, J. V., Remer, L. A., Krotkov, N. A., Tabacniks, M. H., Ben-Ami, Y., & Artaxo, P. (2014). Optical, microphysical and compositional properties of the Eyjafjallajökull volcanic ash. *Atmospheric Chemistry and Physics*, *14*(19), 10,649–10,661. https://doi.org/10.5194/acp-14-10649-2014

Scarnato, B. V., Vahidinia, S., Richard, D. T., & Kirchstetter, T. W. (2013). Effects of internal mixing and aggregate morphology on optical properties of black carbon using a discrete dipole approximation model. *Atmospheric Chemistry and Physics*, *13*(10), 5089–5101. https://doi.org/10.5194/acp-13-5089-2013

Schindelin, J., Arganda-Carreras, I., Frise, E., Kaynig, V., Longair, M., Pietzsch, T., et al. (2012). Fiji: An open-source platform for biological-image analysis. *Nature Methods*, *9*(7), 676–682. https://doi.org/10.1038/nmeth.2019

Schneider, C. A., Rasband, W. S., & Eliceiri, K. W. (2012). NIH image to ImageJ: 25 years of image analysis. *Nature Methods*, *9*(7), 671–675. https://doi.org/10.1038/nmeth.2089

Schuster, G. L., Lin, B., & Dubovik, O. (2009). Remote sensing of aerosol water uptake. *Geophysical Research Letters*, *36*, L03814. https://doi.org/10.1029/2008GL036576

Schwarz, J. P., Spackman, J. R., Fahey, D. W., Gao, R. S., Lohmann, U., Stier, P., et al. (2008). Coatings and their enhancement of black carbon light absorption in the tropical atmosphere. *Journal of Geophysical Research*, *113*, D03203. https://doi.org/10.1029/2007JD009042

Shi, Z., He, K., Xue, Z., Yang, F., Chen, Y., Ma, Y., & Luo, J. (2009). Properties of individual aerosol particles and their relation to air mass origins in a south China coastal city. *Journal of Geophysical Research*, *114*, D09212. https://doi.org/10.1029/2008JD011221

Singh, M., Misra, C., & Sioutas, C. (2003). Field evaluation of a personal cascade impactor sampler (PCIS). *Atmospheric Environment*, *37*(34), 4781–4793. https://doi.org/10.1016/j.atmosenv.2003.08.013

Smith, G. E., Bawa, Z., Macklin, Y., Morbey, R., Dobney, A., Vardoulakis, S., & Elliot, A. J. (2015). Using real-time syndromic surveillance systems to help explore the acute impact of the air pollution incident of March/April 2014 in England. *Environmental Research*, *136*, 500–504. https://doi.org/10.1016/j.envres.2014.09.028

Sobanska, S., Falgayrac, G., Rimetz-Planchon, J., Perdrix, E., Brémard, C., & Barbillat, J. (2014). Resolving the internal structure of individual atmospheric aerosol particle by the combination of Atomic Force Microscopy, ESEM-EDX, Raman and ToF-SIMS imaging. *Microchemical Journal*, *114*, 89–98. https://doi.org/10.1016/j.microc.2013.12.007

Stamnes, K., Tsay, S.-C., Wiscombe, W., & Jayaweera, K. (1988). Numerically stable algorithm for discrete-ordinate-method radiative transfer in multiple scattering and emitting layered media. *Applied Optics*, *27*(12), 2502–2509. https://doi.org/10.1364/AO.27.002502

Sullivan, R. C., Guazzotti, S. A., Sodeman, D. A., & Prather, K. A. (2007). Direct observations of the atmospheric processing of Asian mineral dust. *Atmospheric Chemistry and Physics*, *7*(5), 1213–1236. https://doi.org/10.5194/acp-7-1213-2007

Tan, H., Cai, M., Fan, Q., Liu, L., Li, F., Chan, P. W., et al. (2017). An analysis of aerosol liquid water content and related impact factors in Pearl River Delta. *Science of the Total Environment*, *579*(6), 1822–1830. https://doi.org/10.1016/j.scitotenv.2016.11.167

Tang, M., Cziczo, D. J., & Grassian, V. H. (2016). Interactions of water with mineral dust aerosol: Water adsorption, Hygroscopicity, cloud condensation, and ice nucleation. *Chemical Reviews*, *116*(7), 4205–4259. https://doi.org/10.1021/acs.chemrev.5b00529

Unga, F. (2018). Data for Microscopic observations of core-shell particle structure and implications for atmospheric aerosol remote sensing. https://doi.org/10.17605/OSF.IO/3NZB5

Verleysen, E., De Temmerman, P. J., Van Doren, E., Abi Daoud Francisco, M., & Mast, J. (2014). Quantitative characterization of aggregated and agglomerated titanium dioxide nanomaterials by transmission electron microscopy. *Powder Technology*, *258*, 180–188. https://doi.org/10.1016/j.powtec.2014.03.010

Veselovskii, I., Goloub, P., Podvin, T., Bovchaliuk, V., Derimian, Y., Augustin, P., et al. (2016). Retrieval of optical and physical properties of African dust from multiwavelength Raman lidar measurements during the SHADOW campaign in Senegal. *Atmospheric Chemistry and Physics*, *16*(11), 7013–7028. https://doi.org/10.5194/acp-16-7013-2016

Vieno, M., Heal, M. R., Twigg, M. M., MacKenzie, I. A., Braban, C. F., Lingard, J. J. N., et al. (2016). The UK particulate matter air pollution episode of March–April 2014: More than Saharan dust. *Environmental Research Letters*, *11*(4), 044004. https://doi.org/10.1088/1748-9326/11/4/044004

Wu, Y., Cheng, T., Zheng, L., & Chen, H. (2016). Models for the optical simulations of fractal aggregated soot particles thinly coated with non-absorbing aerosols. *Journal of Quantitative Spectroscopy and Radiative Transfer*, *182*, 1–11. https://doi.org/10.1016/j.jqsrt.2016.05.011

Yang, P., Gao, B.-C., Wiscombe, W. J., Mishchenko, M. I., Platnick, S. E., Huang, H.-L., et al. (2002). Inherent and apparent scattering properties of coated or uncoated spheres embedded in an absorbing host medium. *Applied Optics*, *41*(15), 2740–2759. https://doi.org/10.1364/AO.41.002740

Yin, J. Y., & Liu, L. H. (2010). Influence of complex component and particle polydispersity on radiative properties of soot aggregate in atmosphere. *Journal of Quantitative Spectroscopy and Radiative Transfer*, *111*(14), 2115–2126. https://doi.org/10.1016/j.jqsrt.2010.05.016

Young, G., Jones, H. M., Darbyshire, E., Baustian, K. J., McQuaid, J. B., Bower, K. N., et al. (2016). Size-segregated compositional analysis of aerosol particles collected in the European Arctic during the ACCACIA campaign. *Atmospheric Chemistry and Physics*, *16*(6), 4063–4079. https://doi.org/10.5194/acp-16-4063-2016

Zhang, D., Shi, G. Y., Iwasaka, Y., & Hu, M. (2000). Mixture of sulfate and nitrate in coastal atmospheric aerosols: Individual particle studies in Qingdao (36°04′N, 120°21′E), China. *Atmospheric Environment*, *34*(17), 2669–2679. https://doi.org/10.1016/S1352-2310(00)00078-9

Zhang, K., O'Donnell, D., Kazil, J., Stier, P., Kinne, S., Lohmann, U., et al. (2012). The global aerosol-climate model ECHAM-HAM, version 2: Sensitivity to improvements in process representations. *Atmospheric Chemistry and Physics*, *12*(19), 8911–8949. https://doi.org/10.5194/acp-12-8911-2012

Zuberi, B., Johnson, K. S., Aleks, G. K., Molina, L. T., Molina, M. J., & Laskin, A. (2005). Hydrophilic properties of aged soot. *Geophysical Research Letters*, *32*, L01807. https://doi.org/10.1029/2004GL021496